Tampere University

Md Ehasanul Hoque

THE OPERATIONAL FLEXIBILITY OF VSC-HVDC LINKS FOR CONNECTING WIND FARMS TO DISTRIBUTION SYSTEMS

Master's Thesis
Faculty of Information Technology
and Communication Sciences
Professor Enrique Acha
Professor Pertti Järventausta
December 2020

ABSTRACT

Md Ehasanul Hoque: The operational flexibility of VSC-HVDC links for connecting wind farms to distribution systems.
Master's thesis
Tampere University
Master's Degree Program in Electrical Engineering
December 2020

The penetration of renewable energy technologies (RES), electrical vehicles (EVs) and energy storage systems (ESS) into power systems is growing very significantly, aiming at obtaining CO_2 free, 'green' energy. With the advent of modern, high-power solid-state semiconductor valves and bridges, the various power sectors (namely, generation, transmission and distribution) are undergoing rapid transformation, shifting towards hybrid AC-DC power grids. It is expected that such a transformation will enable higher grid stability, flexibility, voltage level independency and much improved power quality. To realise this, the use of voltage source converters-based HVDC (VSC-HVDC) links, particularly those geared towards the harnessing of the renewable energy resource, are receiving much attention.

The thesis focuses on power flow modelling and analysis where permanent magnet synchronous generator (PMSG) and squirrel-cage induction generator (SCIG) wind turbines are connected to a representative 5-node power system, using VSC-HVDC links. Several types of HVDC links are considered and the two-level VSC-HVDC link model is realized mathematically, in such a way that it is suitable for incorporation into a power flow formulation. Also, different types of wind turbines are studied, and mathematical models are developed to confirm some of the advantages offered by VSC-HVDC equipment to connect wind turbines into the power system. The Newton-Raphson power flow algorithm is adopted to perform the power flow calculations. MATLAB scripting is used to implement the developed mathematical models. Several test cases are studied using this MATLAB software.

The simulation results confirm that VSC-HVDC links do not only provide great flexibility in controlling active power flow but also in regulating voltage magnitude by either absorbing reactive power from the grid or by injecting reactive power into the grid.

Keywords: HVDC link, two-level-VSC-HVDC, PMSG with VSC-HVDC, SCIG

PREFACE

The research work has been carried out to complete my Master of Science degree in Electrical Engineering (major-smart grid) at the department of Information Technology and Communication Sciences, Tampere University.

First, I would like to express my deepest gratitude to my supervisor Professor Enrique Acha for his invaluable help and his availability throughout the research work. I was passing through a tough time just before starting my thesis. His encouragements and determination to help me figure things out is beyond my expectations. My heartfelt thanks to Professor Acha.

I would also like to thank my wife, Afroja and my family for their love and constant support.

Tampere, 20.12.2020

Md Ehasanul Hoque

CONTENTS

LIST OF FIGURES

LIST OF SYMBOLS AND ABBREVIATIONS

ENTSO	*European Network of Transmission System*
AC	*Alternating Current*
DC	*Direct Current*
HVDC	*High-Voltage Direct Current*
FACTS	*Flexible AC Transmission Systems*
VSC	*Voltage Source Converter*
VSR	*Voltage Source Rectifier*
VSI	*Voltage Source Inverter*
SSPS	*Solid State Phase Shifter*
PWM	*Pulse Width Modulation*
IGBT	*Insulated Gate Bipolar Transistor*
SCR	*Silicon Controlled Rectifier*
GTO	*Gate Turn Off thyristor*
IGCT	*Integrated Gate-Controlled Thyristor*
MOSFET	*Metal Oxide Silicon Field Effect Transistor*
SSTC	*Solid State Tap Changer*
STATCOM	*Static Compensator*
MMC	*Modular Multilevel Converter*
SSSC	*Solid State Series Compensator*
MTDC	*Multi-Terminal DC System*
FC	*Flying Capacitor*
CSC	*Current Source Converter*
UPFC	*Unified Power Flow Controller*
DG	*Distributed Generation*
TSSC	*Thyristor Switched Series Capacitor*
DER	*Distributed Energy Resource*
IPFC	*Interphase Power Flow Controller*
WPGU	*Wind Power Generation Unit*
VFT	*Variable Frequency Transformer*
FSIG	*Fixed Speed Induction Generator*
PMSG	*Permanent Magnet Synchronous Generator*
VSWT	*Variable Speed Wind Turbine*
DFIG	*Doubly Feed Induction Generator*
SCIG	*Squirrel-Cage Induction Generator*
TCSC	*Thyristor Controlled Series Compensator*

θ	*Phase angle*
V	*Voltage*
R	*Resistance*
X	*Inductance*
Z_C	*Surge impedance*
P	*Active power*

Q	*Reactive power*
m_a	*Voltage amplitude modulation index*
B_{eq}	*Converter's equivalent shunt susceptance*
G_{sw}	*Converter's switching conductance*
φ	*Converter's phase shifting angle*

1. REVIEW OF HVDC AND HVAC POWER TRANSMISSION AND POWER DISTRIBUTION

1.1 Introduction

A century ago, most electric loads connected onto the demand side of the network were resistive loads and AC rotating machines, and AC prevailed over DC for the purpose of transporting power from centralized stations over long distances, quite efficiently, by transforming voltage levels. More recently, the integration of distributed generations (DGs), such as renewable sources of electrical power, energy storage systems and electric vehicles have been increasing by leaps and bounds. In addition to this, the demand side is dominated by power electronic loads, which are very sensitive to power quality. In the face of this and to maintain power quality standards, the importance of HVDC equipment, systems and methods is growing steadily.

The HVDC revolution may have started in1954 when the first successful HVDC transmission system, rated at 100KV and 20MW, was commissioned between the Island of Gotland and mainland Sweden. A second milestone in HVDC transmission was achieved again in Sweden in1970, when the use of semiconductors valves in HVDC transmission (150kV,30MW) were used for the first time [1]. At present, we are witnessing the accelerated deployments of HVDC links in many forms and ratings, globally. In particular, over the last two decades, the industry is benefitting from the parallel development of semiconductors switches and bridges, and new control techniques and methods [2]. At present, more than 180 HVDC projects are running globally [3]. After a third milestone in HVDC transmission, also having taken place in Sweden in 2000, with the implementation of the world's first practical VSC-HVDC system, its use in connecting RESs has been actively pursued.

ENTSO's predictions are that no less than 50% integration of RESs will take place at the distribution system-level by 2030 [4]. Such integration of DERs may pose grid stability challenges. Among RESs, PV solar energy and wind energy are gaining great popularity as mainstream source of green energy. More to the point, wind power capacity across the world is expanding at a spiral rate, from 24GW in 2001 to 651GW in 2019 [5]. It is expected that by the end of 2020, wind energy capacity would be 727 GW globally.

The wind resource is highly variable and so is the electrical power output of basic wind power generators, whose output varies in proportion to the available wind speed. Therefore, over-voltages, over-loading, voltage flicker and an overall degradation in power systems stability, are major negative impacts [6]. VSC-HVDC systems have come forward as a key solution to integrate wind energy into power networks, including low-voltage distribution networks, as they enable the connection of otherwise independent systems, in an asynchronous manner [7]. This has provided the motivation for investigating the power flow of bipolar VSC-HVDC systems and their role in high-voltage and low-voltage power networks in connection with wind power generation.

This chapter outlines the main theoretical concepts of HVDC systems. One question at the forefront of this discussion is, may DC links and DC power overtake AC links and AC power? This crucial question is addressed in this chapter, from the vantage of the subject matter of this thesis.

1.2 AC versus DC power transmission

Bulk-energy transfers and systems interconnections are the main aims of high voltage transmission. The former involves transporting multi-MW bundles of energy from the large generation units to the long distant cities and industrial centres, where power losses is an issue of paramount technical and economic importance. Regarding systems interconnections, two or more systems need to be operated in a perfectly synchronized and stable way [8]. Alternatively, they need to be operated in an asynchronous manner using an HVDC link. To serve the sole purposes of high-energy transmission, three phase HVAC and HVDC transmission system are well-established technologies.

The ability of an AC power transmission to transport power is inherently limited by angular, transient and dynamic stability limits [9]. In any case, these limits imply that AC lines operate at power levels below their thermal limits. A basic equation for assessing power transfers in an AC transmission line is the following:

$$P_{1-2} = \frac{V_1 V_2}{X_{1-2}} sin\,\theta_{1-2}$$

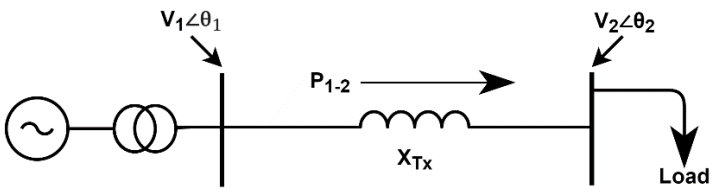

Figure 1.1 : Power transfer in ac transmission line.

where, V_1 and V_2 are the RMS, fundamental frequency, nodal voltage magnitudes, $X_{1\text{-}2}$ is the series reactance and $\theta_{1\text{-}2}$ is the nodal voltage phase angles difference.

Theoretically, a maximum steady-state power transfer occurs at $\theta_{1-2} = 90°$. The line reactance increases with the length of the line; thus, the power transferring ability of an AC overhead transmission line is inversely proportional to its length [10]. As power flow disturbances have a quick and severe effect on the load angle ($\theta_{1\text{-}2}$), this is kept at maximum values of 20° to 30° to avoid angular stability problems [8].

When an AC transmission line is operated at its surge impedance, i.e., natural load, its net reactive power production/consumption is zero. The power transmitted in a transmission line with surge impedance, P_n, is:

$$P_n = \frac{V^2}{Z_c} \qquad Z_C = \sqrt{\frac{L}{C}}$$

where, V is the operating voltage, Z_C is the surge impedance, L is the series inductance per unit length and C is the shunt capacitance per unit length.

Naturally, a HVAC transmission line loaded with its surge impedance and a maximum load angle of, say, 30°, exhibits a physical limitation, namely, the transmission length of the line. For instance, the length l of an AC transmission line with $X = 0.348\Omega/km$ and $\theta = 30°$, may be expressed as a function of the surge impedance, in km:

$$P = \frac{V^2}{X \times l} sin30° = \frac{V^2}{Z_c}$$

$$\frac{1.439 \times V^2}{l} = \frac{V^2}{Z_C}$$

$$l = 1.439 \times Z_C \quad km$$

Thus, to maintain stability, the theoretical length of the line must not be exceeded without some remedial action. Such remedial actions may come in the form of adding series capacitors, shunt reactors or FACTS devices (e.g., SVC, STATCOM, TCSC). Normally, series and shunt VAR compensation are required for transmission lines longer than 300 km operating at 60 Hz, to be able to operate correctly in steady-state.

Alternatively, the electrical energy may be transmitted in DC form, as opposed to AC form. The DC line itself does not exhibit reactance. Hence, angular stability problems and distance limitations are not a concern in DC power transmission, other than power transmission losses.

Corona and radio interference in an AC transmission line is higher than in a DC transmission line of comparable rating. The insulation level employed in an AC transmission line is suitable for use in a DC transmission line in the case of a reconversion [8] [11].

Cables carrying AC current have high capacitance per unit length. Normally, the operating load of submarine and underground AC cables are far lower than the surge impedance, a fact that puts a restriction for lengths exceeding 50km at operating frequencies of 60 Hz [12] . As DC cables are free from capacitive leakage currents, DC cables can carry higher power than AC cables of comparable dimensions.

The interconnection of large AC power grids using AC transmission links is not a straightforward task by any means, due to the risk of large power oscillations, fault level increases and the transfer of frequency disturbances between areas in the interconnected system [9]. Conversely, the interconnection of AC systems using DC links eliminates such difficulties. Two AC power grids linked by a DC link are said to be connected asynchronously. The two power grids may not only be of quite different strengths but also have different operating frequencies, say, 50 Hz and 60 Hz, respectively. That is, the two AC networks being interconnected are not synchronized to each other.

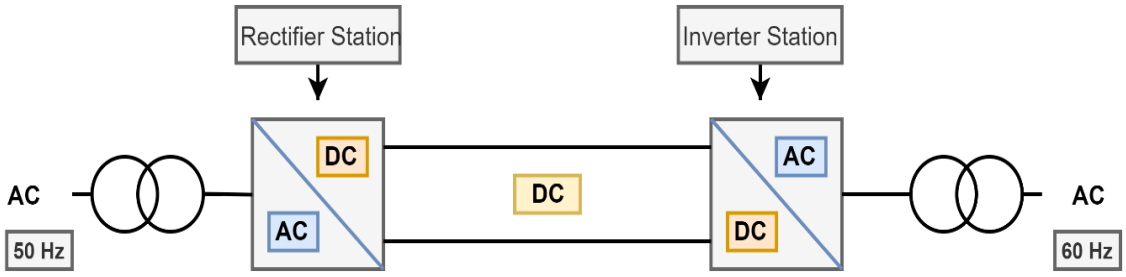

Figure 1.2: Schematic diagram of two interconnected networks via HVDC link.

From an economic vantage, for the same power transmission capacity, a DC transmission line needs less right-of-way than an AC transmission line. It also requires fewer conductors since a three-phase AC transmission line uses three phase conductors whereas a bipolar DC line transmission line uses only two conductors; hence, line cost is cheaper for a DC system. It has to be borne in mind that AC transmission lines longer than 300 km need ancillary reactive power compensation equipment at an intermediate point along the length of the line and that transmission lines longer than 600 km would need two such reactive power compensation substations. However, a DC transmission

line incurs a major infrastructure cost than the AC transmission line does. This is the cost of the rectifier and inverter stations, which represent more than 50% of the overall HVDC system; such an expense is transmission line-independent [11]. Thus, the first perception is that fixed costs are far higher in an HVDC system than an HVAC system of comparable length and rating. However, there is a breakeven distance that varies according to the transmitted power capacity, transmission medium, regulatory requirements etc. Traditionally, the HVDC breakeven distance has been set between 300 km and 800 km for overhead power lines and between 50km and 100 km for power cables [13] [14]. Nonetheless, one ought to bear in mind that the price of high-power, high-voltage power electronics continues to decrease with the passage of time.

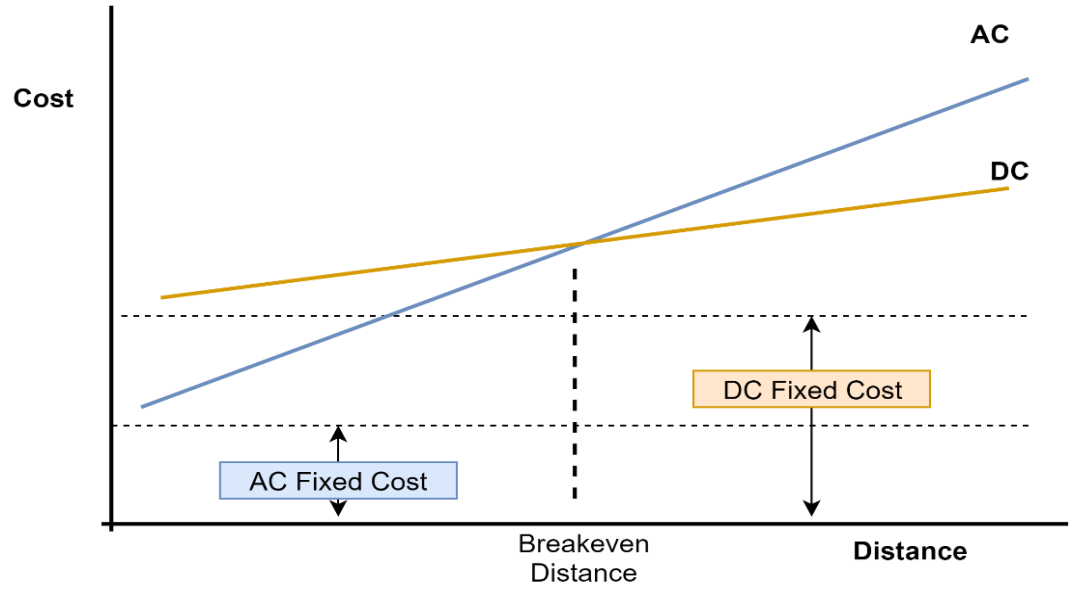

Figure 1.3: Breakeven distance for a HVDC transmission line

1.3 FACTS equipment and HVDC links and their functions in a power system

As discussed, AC power systems benefit greatly from incorporating FACTS and HVDC equipment to control voltage, frequency, active and reactive power and to enable the integration renewable energy sources. The main functions of these technologies in a power network are summarised in Table 1.1.

Table 1.1: Applications of FACTS and HVDC equipment in power system [15]

Devices	Voltage support	Active power support	Reactive power support	Frequency support	AC system interconnection
VSC-HVDC	√	√	√	√	√
CSC-HVDC		√		√	√
VFT		√		√	√
IPFC		√	√	√	
UPFC	√	√	√		
SSSC		√	√		
SSPS		√			
TCSC		√			
TSSC		√			
SSTC	√				
BESS	√		√	√	
STATCOM	√		√		
SVC	√		√		

1.4 Application of VSC-HVDC

Modern power electronics valves, bridges and controls are used not only in power transmission applications but also in power generation and power distribution. The latter are newer applications, which have emerged recently owing to great technical progress and costs reductions.

1.4.1 Generation

Distant power generation units, such as offshore wind farms and remote PV units are ideal candidates to connect to a point of the main AC power grid using a converter-based HVDC links [16]. Battery energy storage systems, although not exactly power generators, use a hybrid, back-to-back HVDC system to connect to the AC power grid.

In wind power generation, the power output of the early generators, termed fixed speed induction generator (FSIG), varies with changes in wind speed. Low steady-state voltage control, limited fault ride through capability, poor power quality, low transient instability margins are some of the limitations exhibited by these early wind power generators [17]. As the wind power industry reached maturity, newer and more powerful wind power generators appeared in the market, fitted with advanced power electronics converters.

Cases in point are the doubly-fed induction machine (DFIM) and the permanent magnet synchronous machine (PMSM) with fully rated converters.

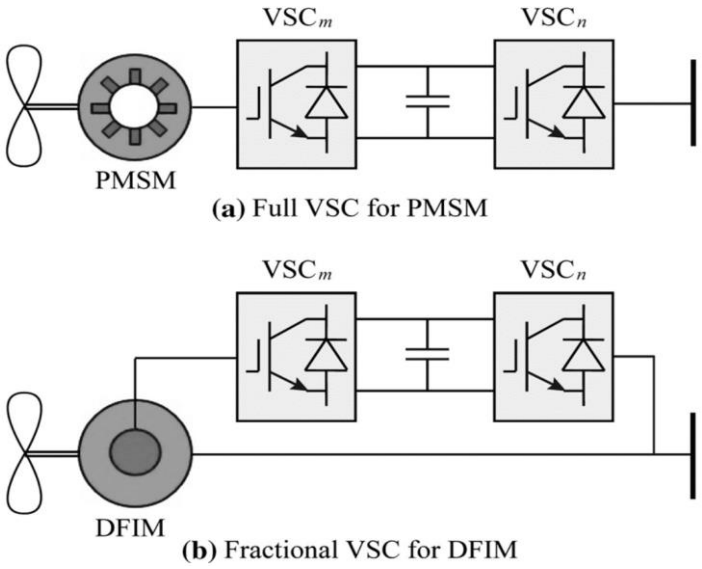

Figure 1.4: Wind turbines using VSCs [18]

In solar PV power plants, the solar generators connect to AC grids via DC/DC boost converters and DC/AC power inverters. This power electronic arrangement is necessary to connect the PV generator to the AC power grid and to provide frequency and voltage support at the point of common coupling. More robust solar power systems can be realized by incorporating an energy storage system with the solar PV generator (Figure 1.5).

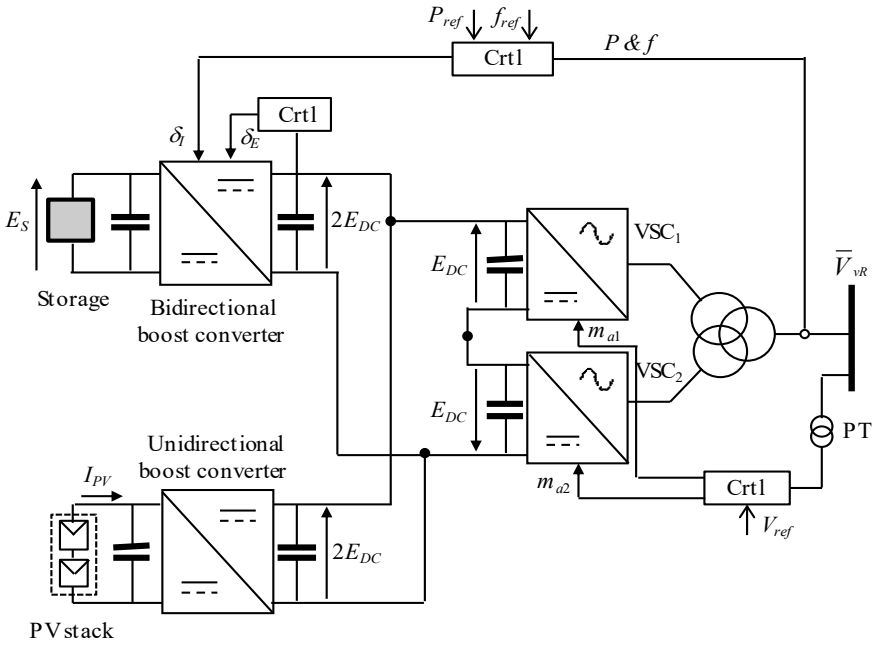

Figure 1.5: Solar power generators with energy storage [15]

During a power system disturbance, the solar PV-battery energy storage system should be able to inject active and reactive power to assist with voltage and frequency support.

1.4.2 Transmission

Existing long-distance HVAC transmission systems may be advantageously converted into HVDC transmission for better power throughputs. For example, a conventional 800MW, 431km long three-phase transmission system (Figure 1.6) can be converted into a compound-bipolar HVDC system using VSCs. Such a reconversion increases at least four-fold the power transfer capacity of the original AC transmission system.

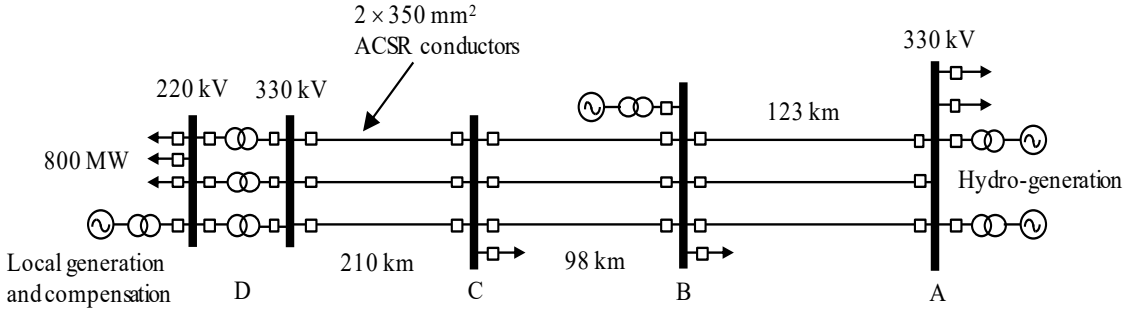

Figure 1.6: Conventional HVAC transmission system [8]

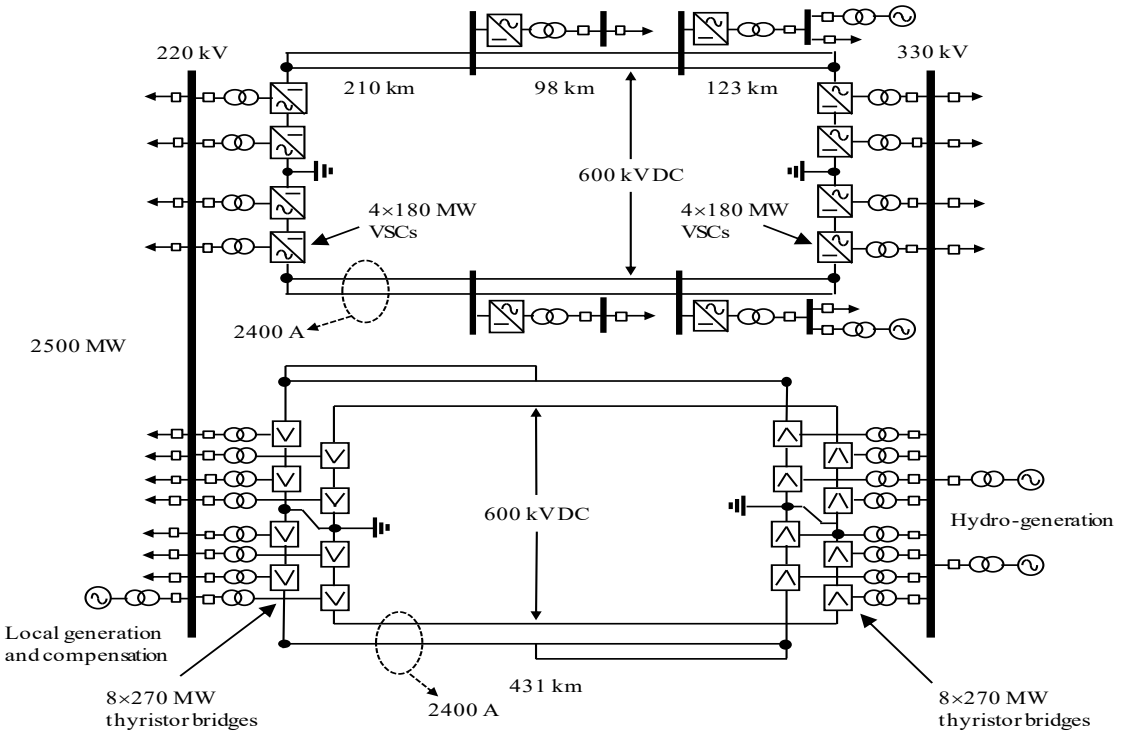

Figure 1.7: Three AC circuit of Figure 1.6 is converted to DC [15]

1.4.3 Distribution

Loads connected into distribution systems are mostly unbalanced and non-linear, which create power quality degradation [19]. The gradual increase of DER installations at the distribution level along with the many power electronic devices at the end-user level possess a threat to power quality. In this respect, VSC-HVDC equipment can be used fruitfully to compensate this situation. In Figure 1.8, a multi-terminal VSC-HVDC is introduced at the end of AC distribution feeder, which transfers regulated active and reactive power via a common DC bus, also enabling the incorporation of a broad range of DC DERs.
In conventional AC distribution feeders, there is a fair chance that the voltage magnitudes at far end of the feeder could be below permissible levels because of natural voltage drops. On the other hand, connecting the generation units at the far end of distribution feeders could rise the voltage magnitudes at common coupling points. To mitigate the poor voltage regulation, low power factor and harmonic pollution, the incorporation of VSC-HVDC systems in distribution networks becomes a most welcome possibility.

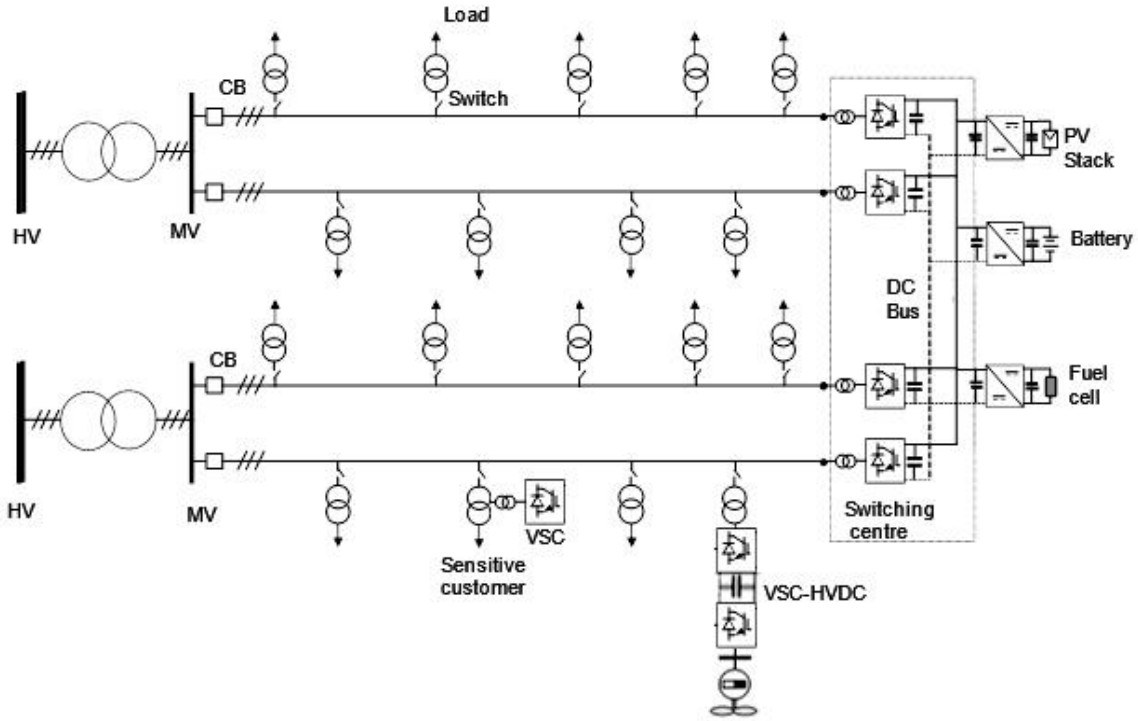

Figure 1.8 : Distribution network with VSC-HVDC.

The distribution system in Figure 1.8 could be transform into a full DC distribution system, in the form illustrated in Figure 1.9. AC loads and power generation units could be connected in a more controllable way using VSI and VSR, respectively.

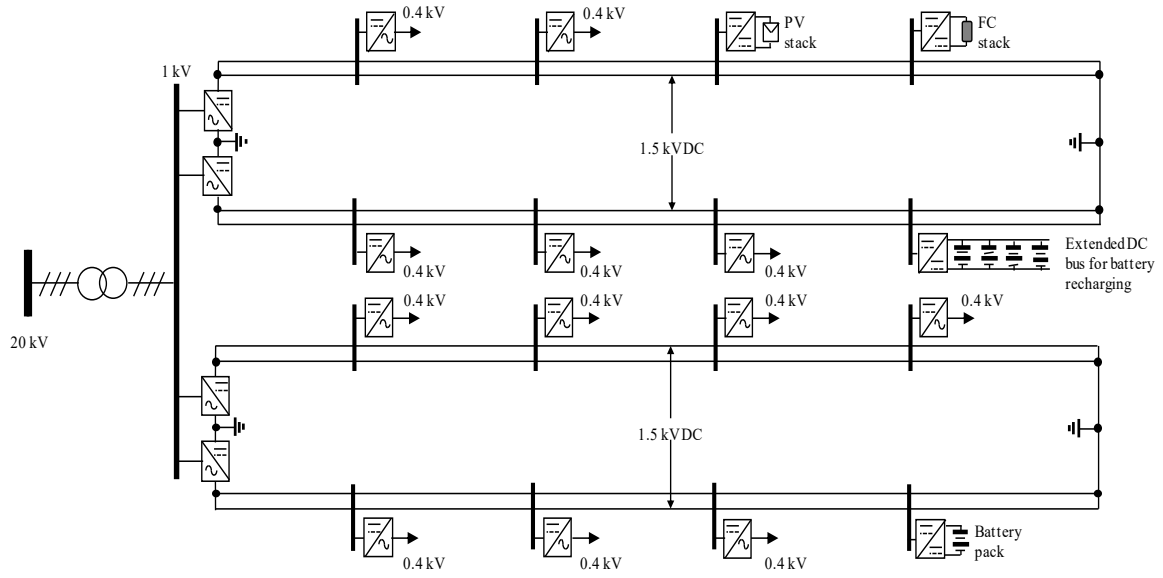

Figure 1.9 : DC distribution system [15]

1.5 Structure of the thesis

This thesis comprises a total six chapters, including this chapter. The structure of the remaining five chapters is given below:

- Chapter 2 discusses the various types of high-power semiconductor switches, which are used today in the power electronics industry. It discusses the two-level, VSC-HVDC configuration, emphasizing its many advantages over the CSC-HVDC configuration.
- In Chapter 3, the grid integration of wind farms at the distribution level is discussed, emphasizing the impact of wind power on power quality. Fixed speed and variable speed wind turbines are elaborated on at this point of the thesis.
- In Chapter 4, the mathematical models of VSC-HVDC, PMSG, SCIG are developed, suitably for incorporation into the Newton-Raphson power flow algorithm.
- Chapter 5 presents case studies and results, where the models developed in Chapter 4 are used to advance our understanding of some of the issues involved in the integration of SCIM-based wind farms and PMSG-based wind farms, into the power grid.
- General conclusion and suggestions for further research work in this area, are pointed out in Chapter 6.

2. MODELLING OF HVDC SYSTEMS

In a HVDC system, at least one power converter is required on each side of the DC link. In principle at least, a power converter can be made to work either as a rectifier (AC to DC) or as an inverter (DC to AC). In order to transfer the electrical energy in the form of direct current and voltage, CSC-HVDC and VSC-HVDC are well-established systems. CSC-HVDC, which is also called classic HVDC, uses thyristor-based current source converters. On the other hand, VSC-HVDC uses IGBT based voltage source converters. This chapter begins with a short overview of power switches, it then progresses to outline the basics of the classic HVDC and VSC-HVDC systems.

2.1 Power electronic switches

The fundamental component of HVDC power converter is the semiconductor valve or switch. The switch selection is application-dependent, it varies according to power handling requirements, current and voltage blocking ratings, thermal rating, firing speed and the type of systems being linked, e.g., a remote hydro plant, an offshore wind park, interconnection of a strong and a weak system. Based on switching control characteristics, power semiconductor switches can be classified as uncontrolled, semi-controlled and full-controlled switches. Examples of the semiconductor valves used today in the high-power, high-voltage applications are shown in Figure 2.1 by means of their symbol representations.

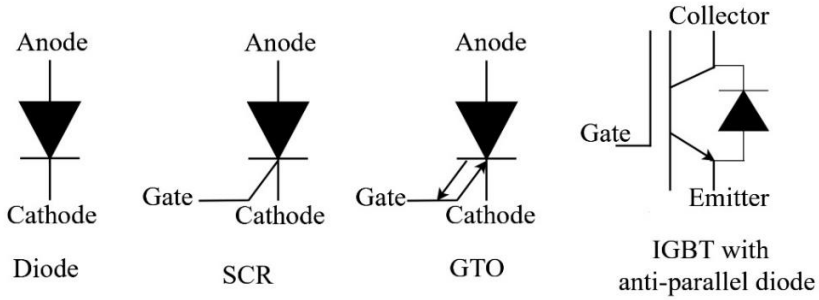

Figure 2.1 : Basic Switches for high power converters

2.1.1 Uncontrolled, Semi-controlled and fully controlled switches

Uncontrolled switches are two terminals with its on/off state governed by the external voltage and current conditions at its terminals. Example of this kind is the diode, which conducts when a small positive voltage exists between its anode and cathode terminals.

The semi-controlled switch has three terminals and is turned-on by applying a pulse current or a light ray at its third terminal. The off state of semi-controlled switches does not depend on external control. These switches are turned-off on their own when their anode current becomes equal to zero [20]. The thyristor or SCR (Silicon controlled Rectifier) and the Triac (Triode ac switch) belong to this category. Despite the limited controllability of the thyristor, it is still extensively used in bulk HVDC transmission because of its extra-high voltage and current rating. In the off state, a modern thyristor has the capability to block positive or negative voltage as large as 7000V and to handle currents in the range of 2000-3000A [21].

Fully controlled semiconductor switches can be tuned on and off by injecting current or voltage pulses to its control terminal. This group contains current driven switches like the Gate Turn Off thyristor (GTO) and the Integrated Gate Controlled Thyristor (IGCT), and voltage driven valves such as the Metal Oxide Silicon Field Effect Transistor (MOSFET), the Bipolar Junction Transistors (BJT), and the silicon carbide MOSFET and IGBT.

2.1.2 Switches for HVDC links

Suitable semiconductor switches for high-power applications with adequate controllability appear to be the following: IGBTs, IGCTs and GTOs. Although the GTO has a higher power rating than the others, its power losses are higher as it requires a snubber network. The ICGT offers lower total power losses than the GTO. Nonetheless, because of switching losses, the ICGT has limited switching speeds of up to 500 Hz for soft-switching operation; it requires a complex gate driver [22]. On the other hand, IGBTs need less gate power and have superior soft-switching frequency up to 3kHz. Besides, IGBTs offer higher reliability as they can inherently tolerate current surges and are even in immune to moderate short circuit conditions. Present day IGBTs have maximum 6.5kV blocking voltages and handle 2.5 kA peak turn-off current [23].

Several IGBTs and their associated fast recovery diodes in antiparallel connection, are press-packed in a single module. The use of press-pack IGBT modules in HVDC systems is progressively escalating on account of their ability to operate in series, their high power rating and their capability to conduct under short-circuit conditions [24]. Some noteworthy press-pack IGBT modules, which are available in the market in 2020, are the following: StakPak BIGT module: 5200V/3000A by ABB [25], T2960BB45E module: 4500V/3000A by Westcode [26], ST2100GXH24A module: 4500V/2100A by TOSHIBA [27], DPI2100P45A5200 module: 4500V/2100A by DYNEX [28].

2.2 CSC-HVDC systems

Classic HVDC systems are traditionally used for bulk power transmission. Thyristor-based current source converters act well both as rectifiers (thyristor firing angle 0°-90°) and as inverters (thyristor firing angle 90°-180°). A six-pulse, three-phase thyristor converter (Figure-2.2) behaves like a constant current source, which absorbs reactive power. It also produces current harmonics on the AC side and voltage ripple on DC side, which significantly reduces by using twelve-pulse configurations.

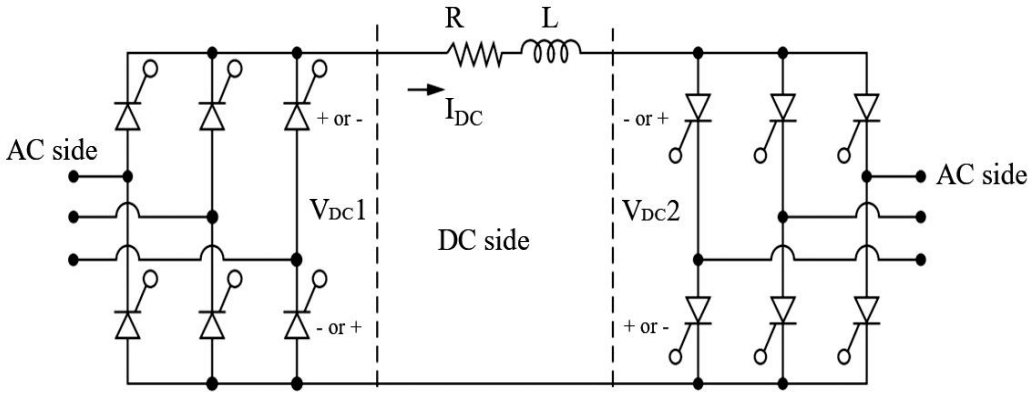

Figure 2.2: Six-pulse three-phase thyristor converters

On the Ac side, passive filters are installed to limit the 6*k*±1 and 12*k*±1 (*k*=1,2,3) harmonic currents produced by 6-pulse and 12-pulse converter bridge, respectively. Ripple on the DC side can be eliminated by active or passive filters [29]. Normally, there is no DC filter required for back-to-back HVDC and for pure cable transmission systems. The most used topology in classic HVDC systems, is the bipolar, point-to-point scheme.

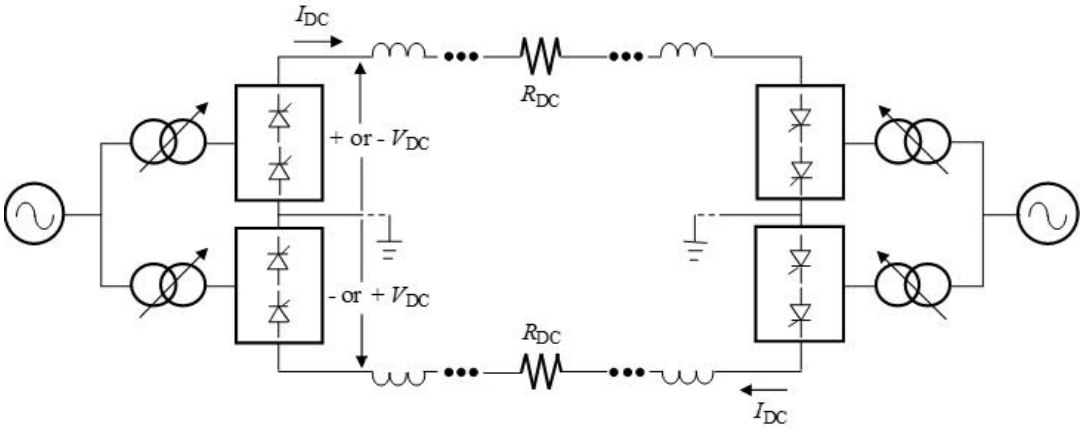

Figure 2.3 : Classic HVDC, point-to-point, bipolar system [15]

Power flow is controlled through the thyristor firing angles and the tap changer transformers. When the voltage is positive, the current flows from the rectifier station to the inverter station and so does the power flow. When the DC voltage polarity is reversed,

the power flows from the inverter to the rectifier – voltage polarity is achieved solely by firing angle control. A communication link is required at both stations. As CSC-HVDC systems depend on current balancing, efficient multi-terminal HVDC systems can only be built in series. To date, this is the major drawback of this flavor of the HVDC technology.

2.3 VSC-HVDC systems

VSC-HVDCs offer a higher degree of controllability in contrast to classic HVDC. As the valves employed are self-commutating, their operation is independent from the external circuit conditions. The active and reactive power flow can be controlled separately. It implies that without changing the active power, the AC side voltage can be controlled automatically via a reactive power controller. Reactive power compensation to the connected AC networks is achievable by using the reactive power generation/absorption capability of both VSC-HVDC converters. Meshed, multi-terminal HVDC grids using VSC converters is a new concept in HVDC transmission; where little communication between converter stations is needed; no dc voltage reversals are needed to change the direction of power flow. These multi-terminal HVDC systems behave more line meshed AC power grids.

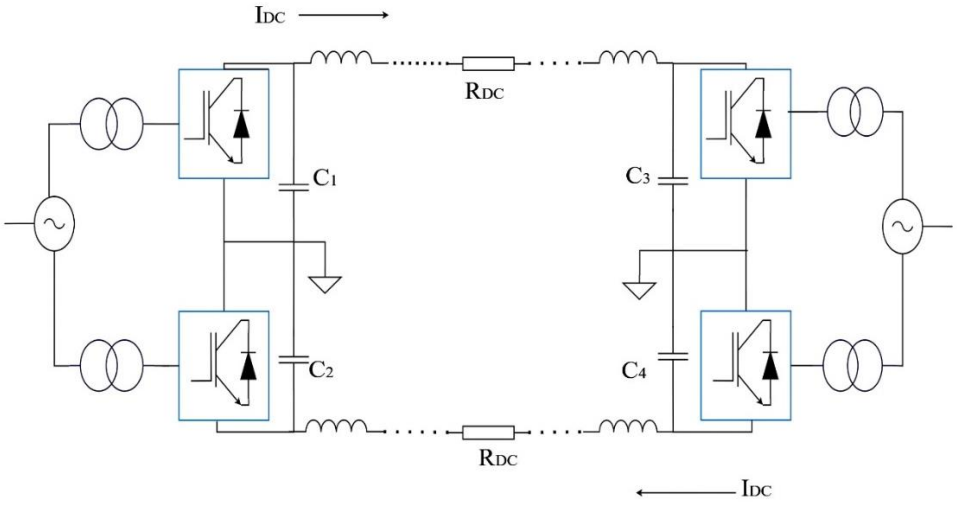

Figure 2.4 : Schematic representation of point-to-point, bipolar VSC-HVDC system

2.4 Structure of VSC-HVDC systems

In VSC-HVDC systems, voltage source converters are used as rectifier and inverter stations where the switches are IGBT. The switching of the IGBTs is driven by PWM control techniques. The PWM control keeps the average voltage constant by varying the width of the high-frequency voltage pulses. Also, some low-order harmonics are eliminated in

this technique. In PWM, a sawtooth or a triangular wave-carrier frequency is compared against a control signal to produce the desired output voltage waveshape.

2.4.1 Single-phase power converters with PWM

In single-phase, full-bridge converters, switches can be driven by bipolar and unipolar PWM voltage switching techniques. Using these schemes, full bridge converter can have output voltage $+V_{DC}$, 0 and $-V_{DC}$.

In the bipolar scheme, as shown in Figure 2.5, ON and OFF state of T_A^+, T_B^- and T_A^-, T_B^+ are governed with the control signal and triangular signal. When $V_{tri} > V_{control}$, T_A^+ and T_B^- is ON, $v_{A0} = \frac{V_{DC}}{2}$ and $v_{B0} = -\frac{V_{DC}}{2}$ hence $v_0 = V_{DC}$, similarly for $V_{tri} < V_{control}$ T_A^- and T_B^+ is on, $v_0 = -V_{DC}$.

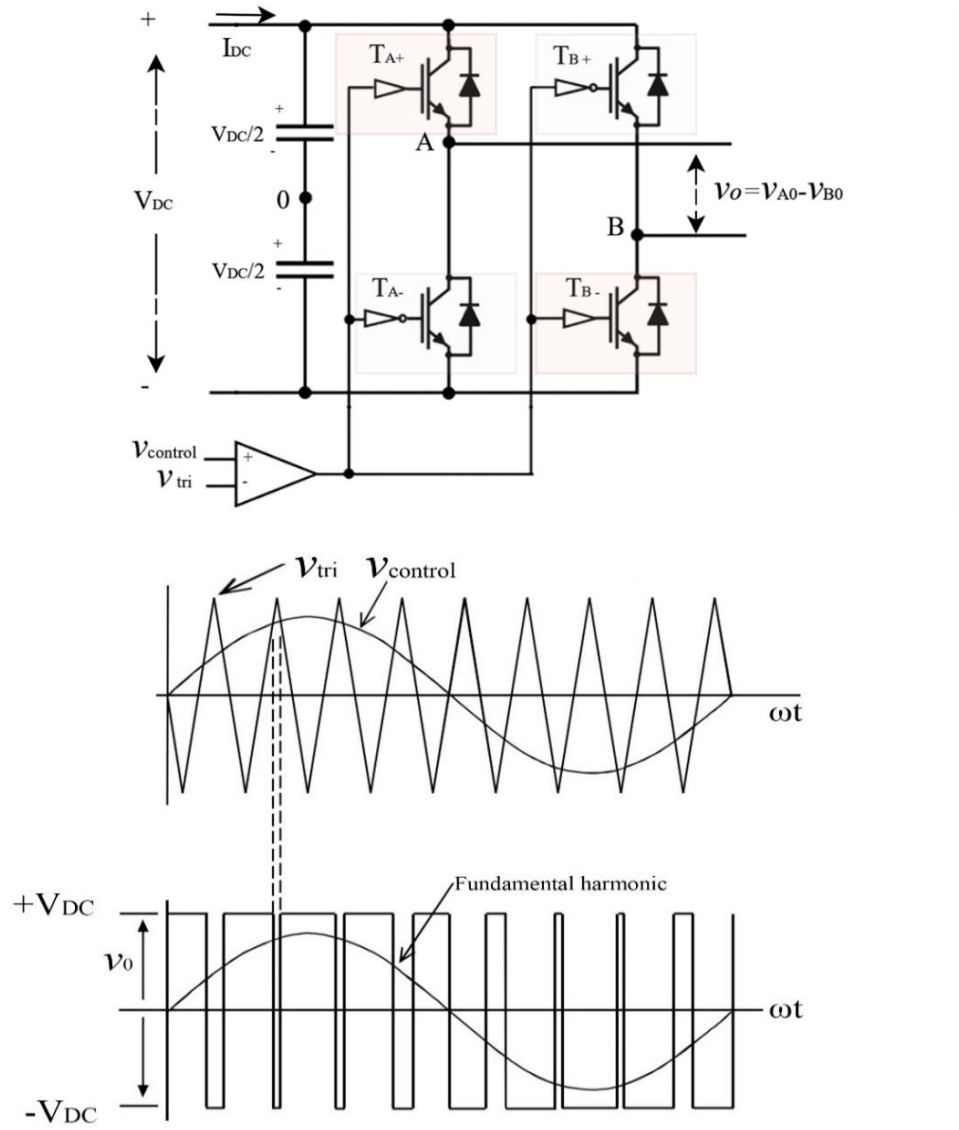

Figure 2.5 : Single phase inverter with bipolar switching and its output (ma= 0.8 and mf= 9) [30]

In unipolar scheme (Figure 2.5), two control signals are used which have 180° phase difference. T_A^+ and T_A^- are controlled by comparing $+V_{control}$ and V_{tri}. T_B^+ and T_B^- are driven by $-V_{control}$ and V_{tri}.

$V_{control} > V_{tri}$: T_A^+ ON, $v_{AN} = V_{DC}$; $-V_{control} < V_{tri}$: T_B^- ON, $v_{BN} = 0$; $v_0 = V_{DC}$

$V_{control} < V_{tri}$: T_A^- ON, $v_{AN} = 0$; $-V_{control} > V_{tri}$: T_B^+ ON, $v_{BN} = V_{DC}$; $v_0 = -V_{DC}$

$V_{control} > V_{tri}$: T_A^+ ON, $v_{AN} = V_{DC}$; $-V_{control} > V_{tri}$: T_B^+ ON, $v_{BN} = V_{DC}$; $v_0 = 0$

$V_{control} < V_{tri}$: T_A^- ON, $v_{AN} = 0$; $-V_{control} < V_{tri}$: T_B^- ON, $v_{BN} = 0$; $v_0 = 0$

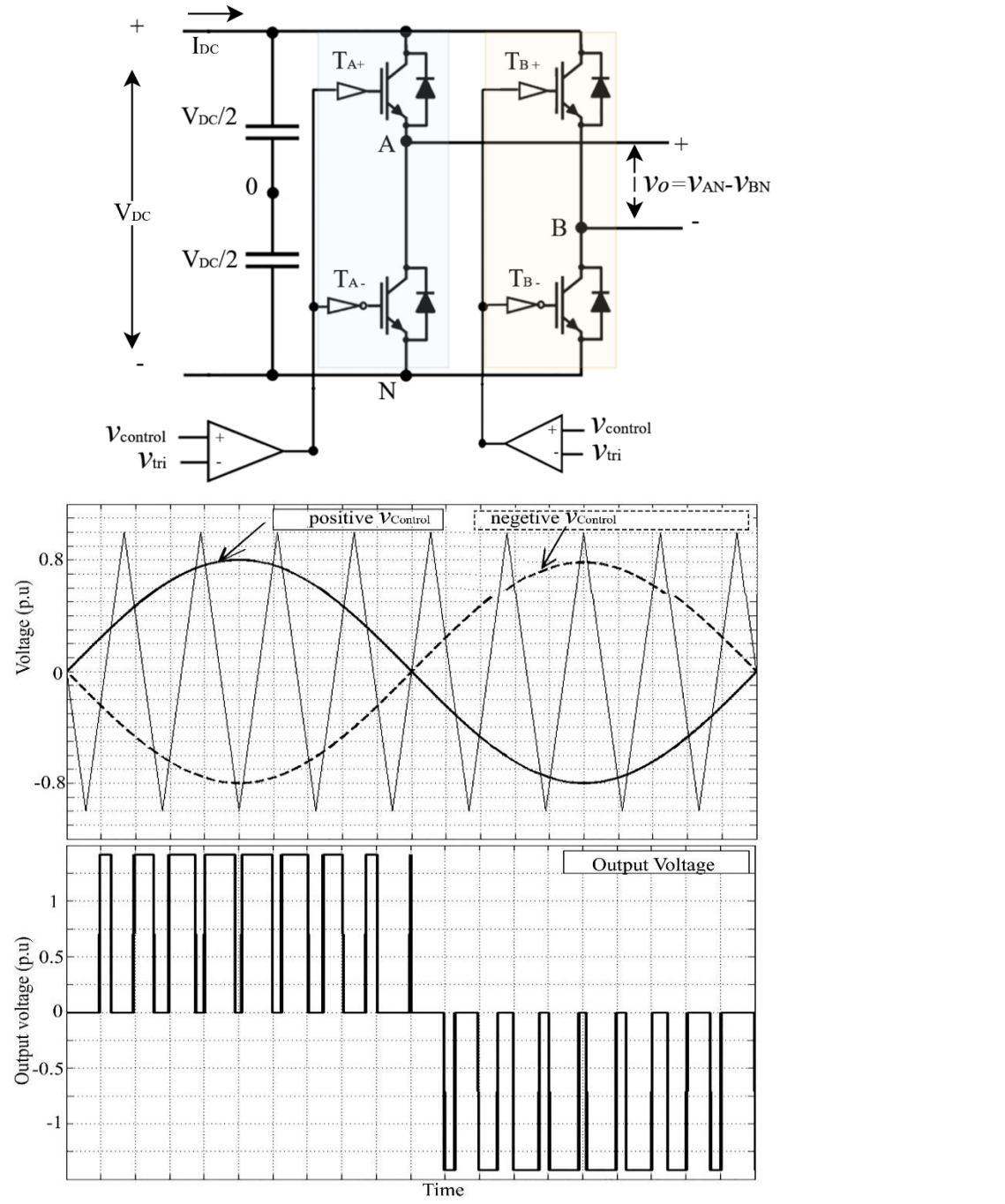

Figure 2.6 Single phase inverter with unipolar switching and its output (ma= 0.8 and mf= 9) [30]

In both PWM schemes, the magnitude of the fundamental frequency output voltage, $\hat{V}_0 = ma\, V_{DC}$ and the frequency is the same as those of the control signal. Here, ma is called amplitude modulation index, which is the ratio of the peak amplitude of control signal and triangular carrier signal.

$$ma = \frac{\hat{V}_{control}}{\hat{V}_{tri}}$$

The frequency of the triangular signal is known as switching or carrier frequency. The desired fundamental frequency of the output voltage depends on the frequency of control signal. The ratio of the frequency of carrier signal and control signal is called frequency modulation index (mf).

$$mf = \frac{switching\ frequency, f_{tri}}{desired\ frequency, f_{control}}$$

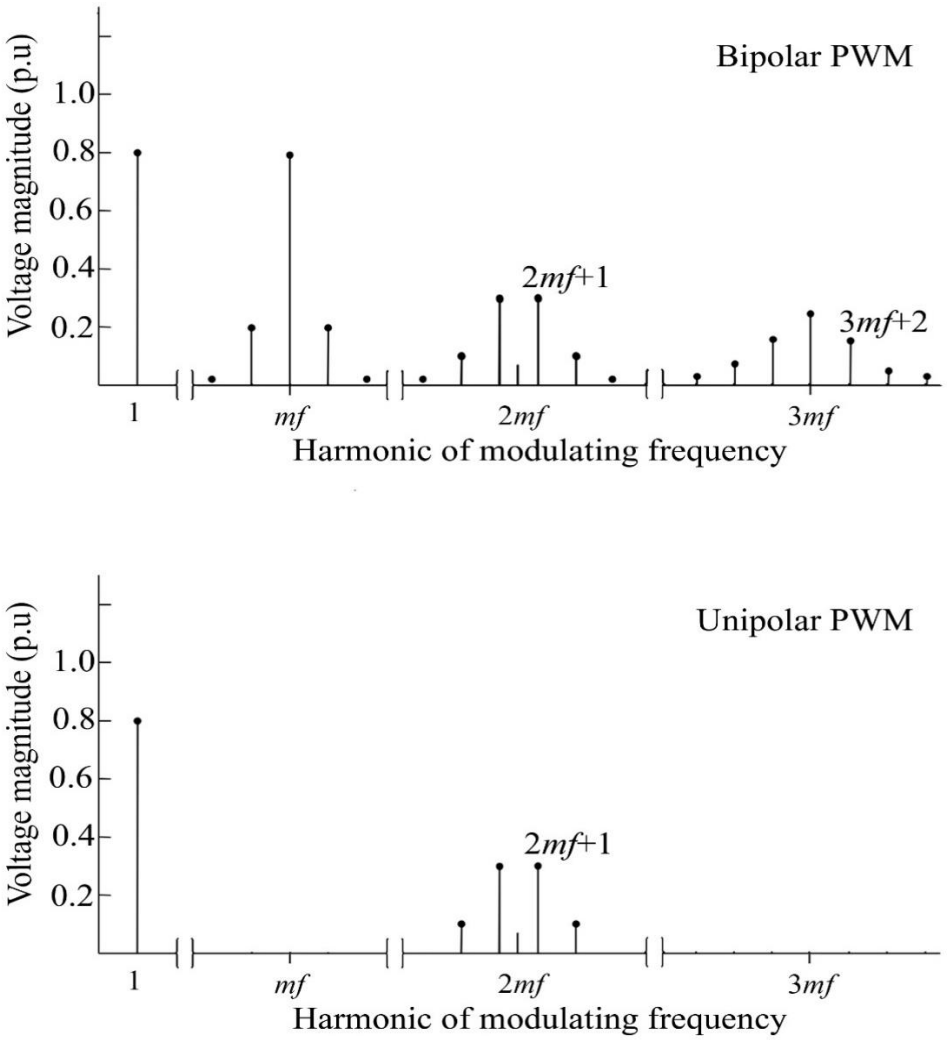

Figure 2.7: Single phase full bridge frequency spectrum, bipolar and unipolar (ma = 0.8 and mf= 9) [30]

In the linear region ($ma \leq 1$), the amplitude of the fundamental output voltage, $\hat{V}_0$ varies linearly with the DC side voltage, $\mathrm{V_{DC}}$. Varying the amplitude of $\mathrm{V_{control}}$, the output voltage is kept constant despite variations in $\mathrm{V_{DC}}$. Harmonic frequencies do exist in the output voltage at multiples of the switching frequency, with sidebands cantered around the respective harmonic. The higher switching frequency the higher the frequency value at which the harmonics start appearing, which leads lowering needs of filtering requirements. However, higher switching frequency causes higher switching power losses. Notably, that amplitude of harmonics is independent of the mf value. The presence of even harmonics in the output voltage is eliminated by setting mf to have an odd integer value. In unipolar switching, the effective switching frequency is doubled; hence, the first harmonic appears as sideband at $2\mathrm{mf}$. Odd harmonics at switching frequency and its multiples are not present in unipolar PWM, as shown in Figure 2.7.

Setting $ma > 1$, the fundamental frequency output voltage can be greater than the input voltage. The trade-off for this is that no control of the output voltage magnitude is possible, and all the odd harmonics become present.

When $ma \gg 1$, the inverter works in the square-wave mode. In this range, the switches are turned on only twice per cycle. The desired output voltage magnitude can be achieved by only adjusting the inverter's dc side voltage, $\mathrm{V_{DC}}$. The maximum achievable amplitude of the fundamental output voltage ca be $\hat{V}_0 = ma\ \frac{4}{\pi}\ V_{DC}$.

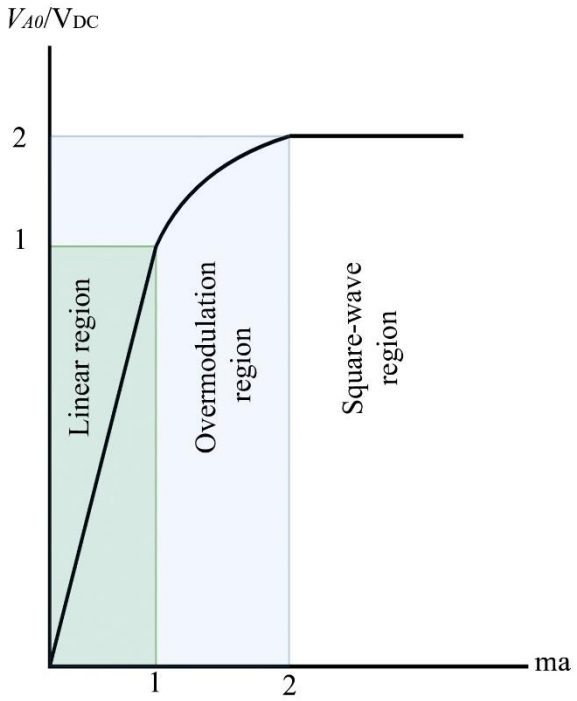

Figure 2.8: Single phase voltage as a function of ma (mf=9).

2.4.2 Three-phase power converters with PWM

Three-phase, two-level voltage source inverters are most frequently used in high-power transmission networks. It includes three legs and six valves. Each leg is controlled by control signals which are 120° out of phase.

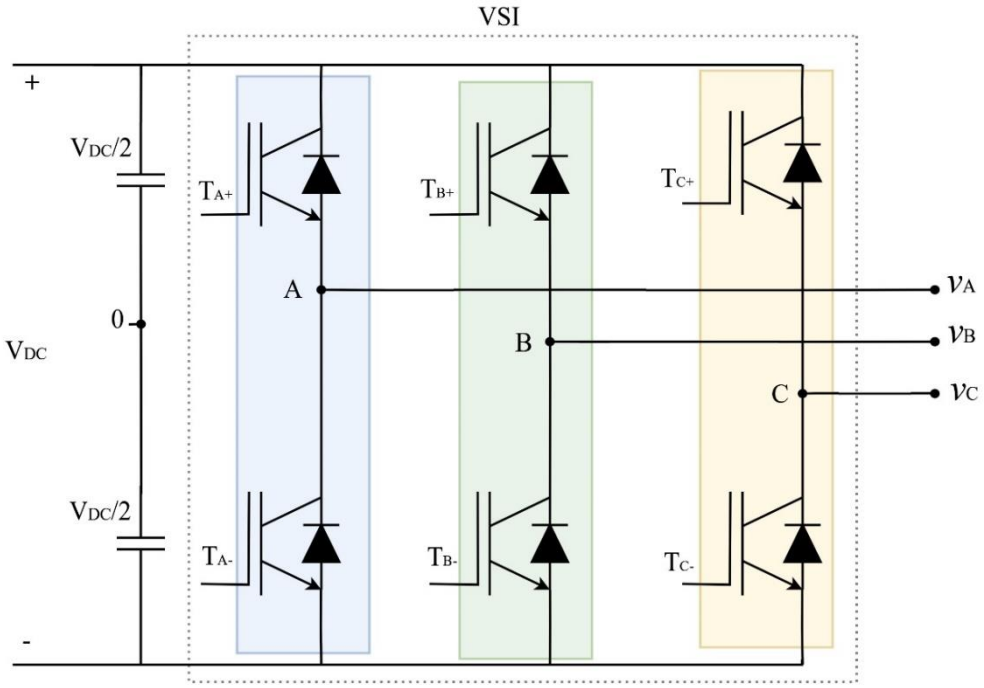

Figure 2.9: Two-level, three-phase inverter

The average DC components of legs v_{AN}, v_{BN}, v_{CN} are equal and cancel out each other in the line-to-line voltages (e.g: v_{AB}). The peak magnitude of the fundamental frequency output voltages are identical, which is $\hat{V}_{AN} = \hat{V}_{BN} = \hat{V}_{CN} = ma\ \frac{V_{DC}}{2}$ (Phase).

The peak magnitude of the line-line fundamental output voltage, $\hat{V}_{LL} = \sqrt{3}\ \times ma\ \frac{V_{DC}}{2}$.

$= \frac{\sqrt{3}}{\sqrt{2}} \times ma\ \frac{V_{DC}}{2}$ (in R.M.S)

The harmonic at mf and its multiple have the phase difference (120× mf) ° in the output voltage of each phase. Selecting mf as an odd integer or a multiple of 3 significantly reduces the harmonic content in the line-line voltage [31].

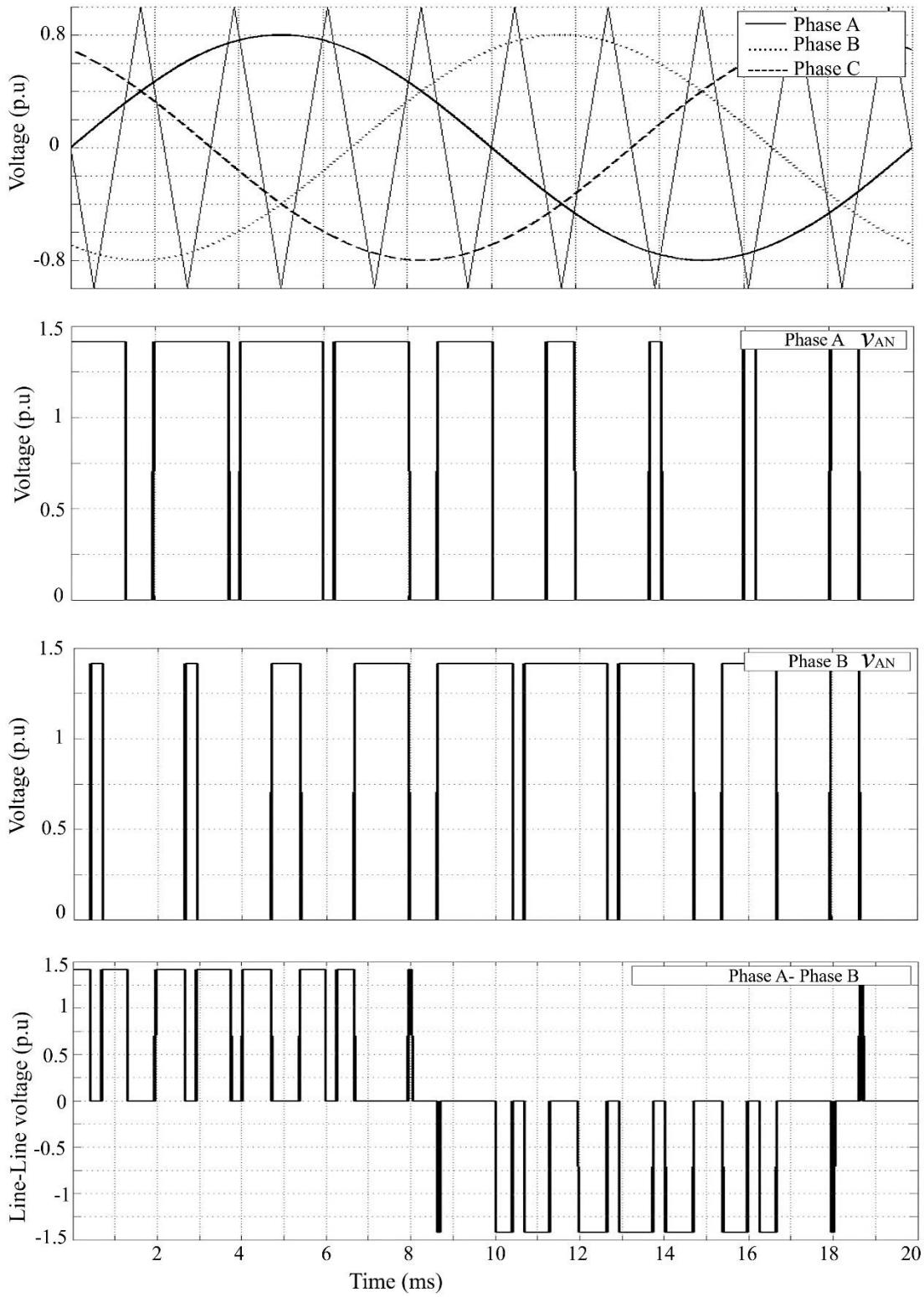

Figure 2.10 : Two-level, three-phase inverter PWM waveforms (ma=0.8 and mf= 9) [30]

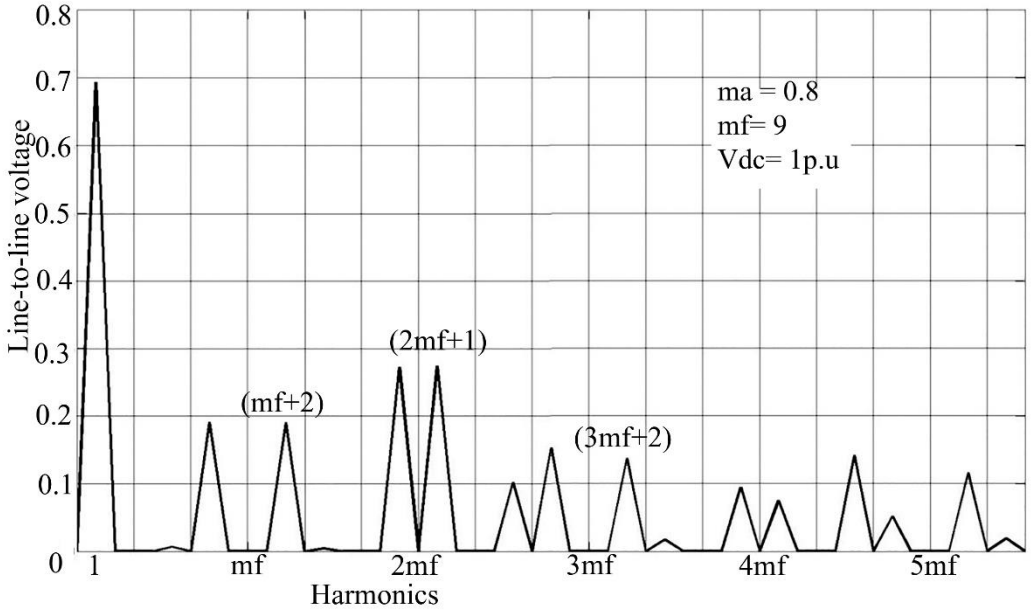

Figure 2.11 : Frequency spectrum of three-phase inverter (line-line) [30]

2.4.3 Modular Multi-level Converters

In high power applications, multilevel VSCs represent a possible solution to overcome the limitations of two-level VSCs, such as high switching power loss, high $\frac{di}{dt}$ and $\frac{dv}{dt}$ and the presence of high frequency harmonics [32]. Neutral-point-clamped (NPC), cascade half-bridge converters, flying capacitor (FC), modular multilevel converters (MMC) are all well-known multilevel VSC topologies. For achieving high number of voltage level in NPC, a high number of clamping diodes are required, which creates voltage balancing complications [33]. Similarly, for flying capacitor (FC), control and construction of the inverter becomes challenging as a large number of capacitors are required [33], [34]. MMC VSC, as shown in Figure 2.12, which was introduced in 2003 [35], has drawn great attention because of its higher scalability and modularity, lower switching loss than two-level voltage converters [34], [36] .

Three-phase MMC consists of n-number of series connected power unit (PU), which are basically half-bridge converters. MMC can produce nearly sinusoidal voltage waveshapes by increasing the number of PUs. It is accomplished by balancing the voltages of the individual PUs at low switching frequencies (100-150Hz). With MMCs power losses of around 1%, whereas losses in two-level and three-level VSCs are around 2% [15].

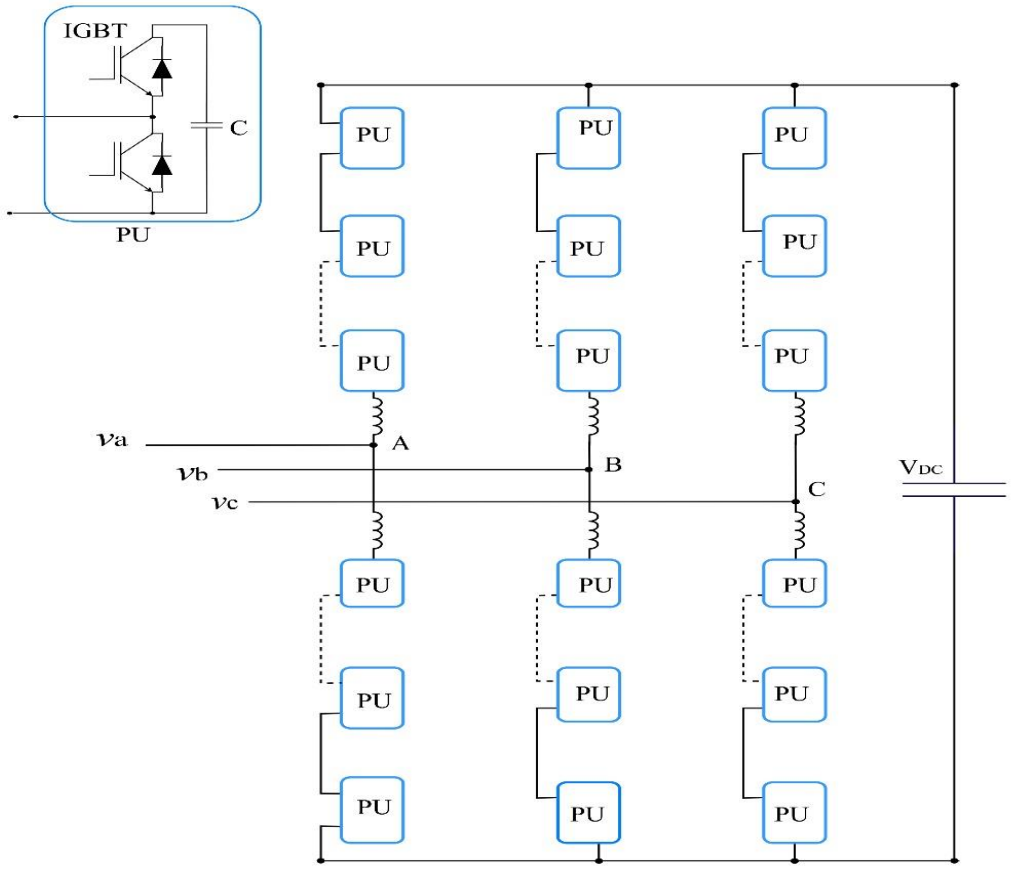

Figure 2.12: Structure of modular multilevel converter (MMC)

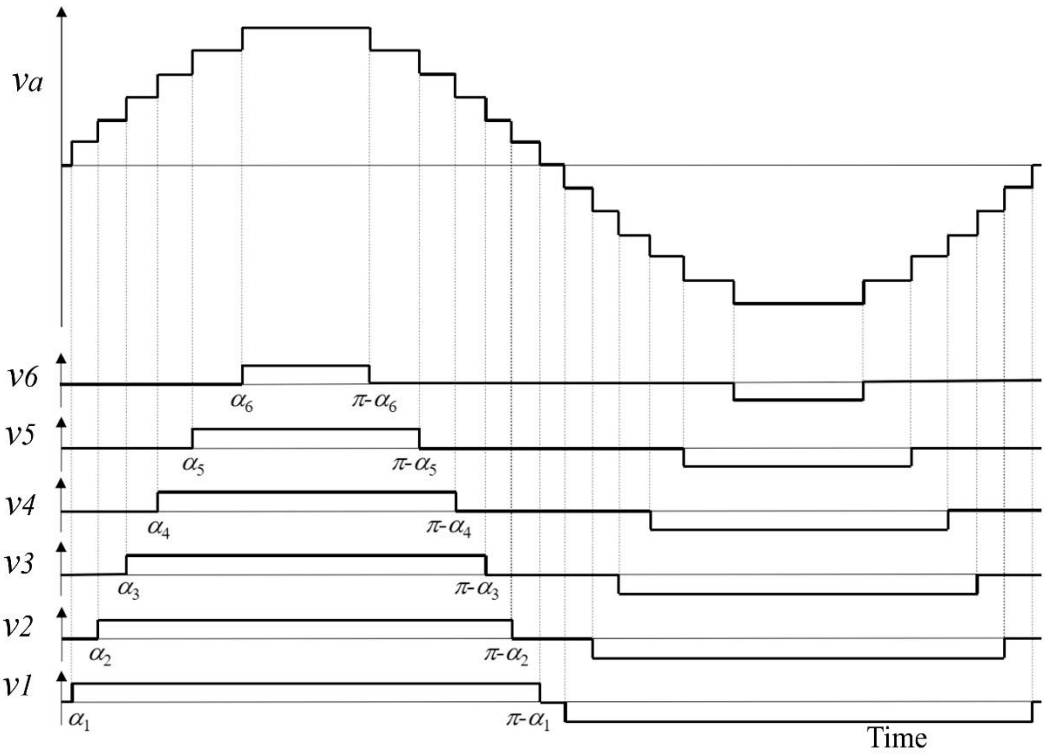

Figure 2.13: Output voltage of MMC [18]

2.5 Possible arrangements of VSC-HVDC systems

The arrangement of VSC converters, controllers, filters, lines and cables is dependent on geographical location, technical requirements and budget. Depending on the requirements, rectifier and inverter stations can be connected either back-to-back or linked by cables (overhead, underground, submarine) or by overhead lines in monopolar or bipolar configurations.

2.5.1 Monopolar Configurations

Two-level or modular multilevel VSCs are connected using a single pole cable or line, which carries either positive or negative DC voltage, as shown in Figure 2.14. Earth or metallic return conductor or fully insulated cables are used as return path of the current. The loss of redundancy for full power is the main drawback of the monopolar connection.

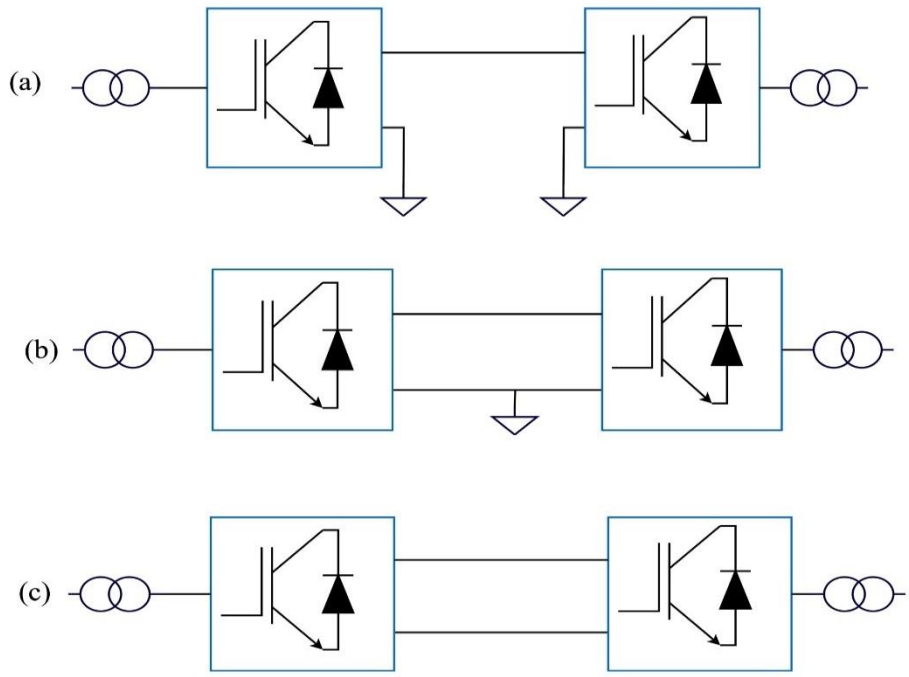

Figure 2.14 : : Monopolar configuration with (a) ground return, (b) metallic return, (c) symmetric monopole

2.5.2 Bipolar Configurations

A bipolar connection, as shown in Figure 2.4, consist of two monopolar asymmetric links, one has positive and the other has negative voltage polarity with reference to ground. Bipolar HVDC links has double power carrying capacity than monopolar HVDC links. Each unit can operate independently owning to separate ground returns. When both poles operate together in normal condition, there is no ground current return because

there are equal currents flowing through in each link. This configuration offers better reliability as power transmission continues even when one pole is out of service; with the bipolar link operating at 50% capacity.

2.5.3 Back-to-Back VSC-HVDC links

This scheme is also called zero-distance VSC-HVDC, as illustrated in Figure 2.15, where two VSCs are linked back-to-back (no cable exists). It enables asynchronous interconnection between two neighbouring systems with different power frequency. It is also used for splitting up a very strong network to reduce its short circuit current.

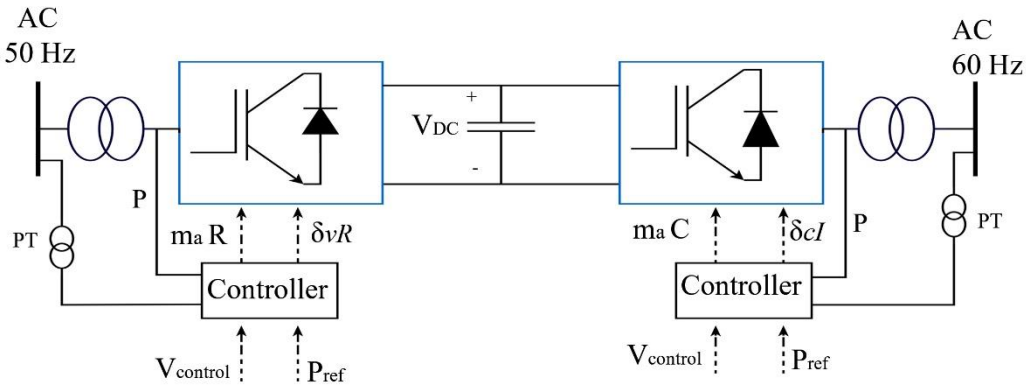

Figure 2.15: monopolar, back-to-back VSC- HVDC scheme

2.5.4 Point-to-point VSC-HVDC links

In this configuration, as shown in Figure 2.4 and 2.16, a rectifier station is connected to a distant inverter station, which can be hundreds of kilometres apart, to transmit bulk power. The nominal frequency of the two interconnected AC systems may be the same or not. As VSCs are capable to regulate the voltage level quickly, the connecting transformers do not necessarily need to have tab-changing options.

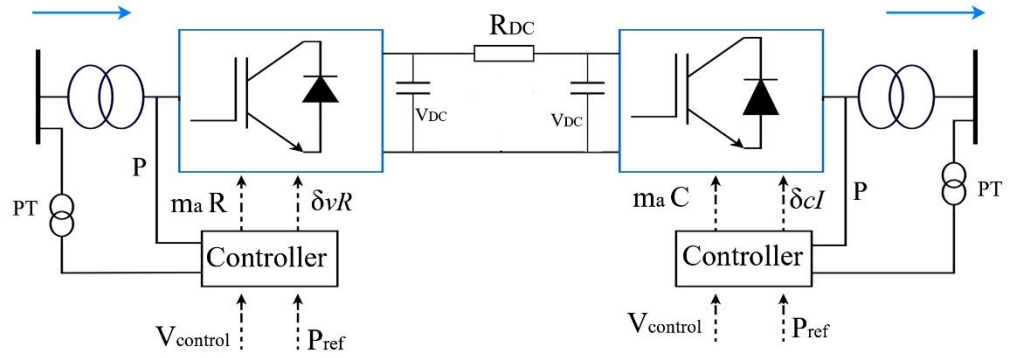

Figure 2.16 : Monopolar, point-to-point VSC-HVDC scheme

2.5.5 Multi-Terminal VSC-HVDC systems

In MT-VSC-HVDC systems, more than two VSCs are interconnected by lines or cables to form a radial or a meshed DC network. A schematic representation of a meshed, four-terminal VSC-HVDC system is shown in Figure 2.17 [11] . With fast advancements of VSC-HVDC, it is expected that multi-terminal DC systems (MTDC) will be exist in the near future at transmission and distribution levels [3] [37]. However, the practical implementation of MT-VSC-HVDC is challenging due to its operational and controlling complexity, which need to be overcome by further research and investment in all aspects of the MT-VSC-HVDC technology. Some of the challenges surrounding this technology are: power flow control, system integration, dynamic behaviour, stability issues, effective HVDC circuit breaker development [3].

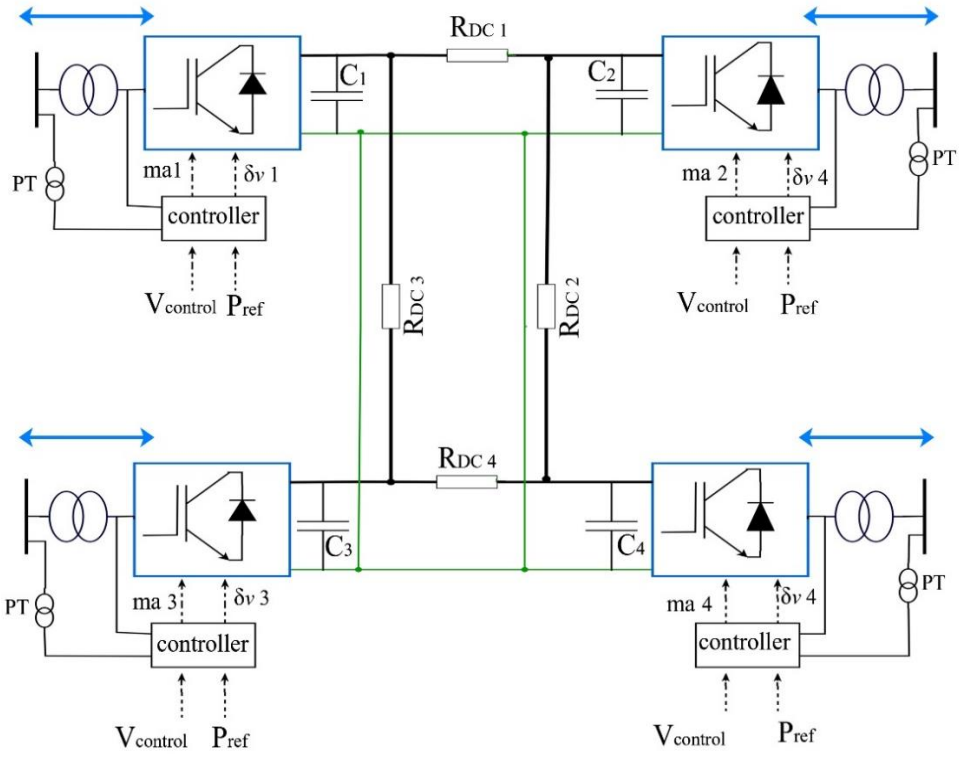

Figure 2.17 : Typical example of a four-terminal VSC-HVDC system

2.6 Conclusion

Bearing in mind current progress of in semiconductor switches, it is expected that new converter topologies, with higher efficiency than what we have today, will be introduced in near future. By incorporating future power converters, existing three-phase radial distribution systems would become more flexible and capable to integrate decentralized

generation units and other DERs (e.g: BESS, EVs). Use of VSC-HVDC in low-voltage distribution systems, especially multi-terminal HVDC systems, would be a breakaway solution in the area of power delivery, as they provide full flexibility, higher power throughputs and much reduced power losses.

3. WIND ENERGY

Wind speed varies significantly from one location to next. To harness the wind energy, large-scale and small-scale wind farms are being built in all corners of the world, to power homes, factories and offices.

3.1 Major challenges in the integration of wind turbines in a distribution system

As the penetration levels of wind power increases, issues regarding power quality, reliability of supply and system stability, are receiving much attention. Connecting a wind farm to a weak AC network (low $\frac{X}{R}$ ratio) poses challenges to maintain adequate levels of power quality and continuity of supply. Variable wind speeds cause voltage and frequency variations in the power network; flicker emission may be introduced due to sustained voltage fluctuations. Moreover, overvoltage problem may take place at the common coupling point between the wind farm and the distribution network when the wind farm exceeds its rated power output. The voltage fluctuations due to wind farms can be brought under control by using power electronics equipment of various kinds.

During transient conditions, FSIGs consume large amounts of reactive power resulting from rotor acceleration leading to a possible wind farm disconnection and power network instability. To minimize the occurrence of such an effect, modern wind power generators are required to have fault-ride-through capability. New wind power generators, which are variable speed, should be capable of continuous operation during and after network faults in the vicinity of the wind farm, to overcome voltage dips situations. However, the power converters used in variable speed wind turbines may cause harmonic and interharmonic distortion in the AC power grid.

3.2 Grid code specifications

The grid-connection of wind power generation units (WPGUs) should follow a set of grid specifications. The grid requirements of a WPGU, relating to operational voltage, frequency range, power factor, reactive power and low-voltage ride-through, are dependent on the relevant voltage level. The extent of these mandatory requirements varies from country to country.

A power generation unit is required to maintain its output power at certain, pre-specified level and time span, within agreed ranges of frequency and voltage levels at a point of

common coupling. This is illustrated in generic form in Figure 3.1. For example, in Finland, WPGUs have to run continuously when the system frequency is in the range 49.0-51.0 Hz and should remain operational for a period of 30 minutes when the system frequency is in the ranges 47.5-49.0 or 51.0-51.5 Hz [38]. However, WPGUs may reduce their active power outputs when system frequency drops below 49 Hz.

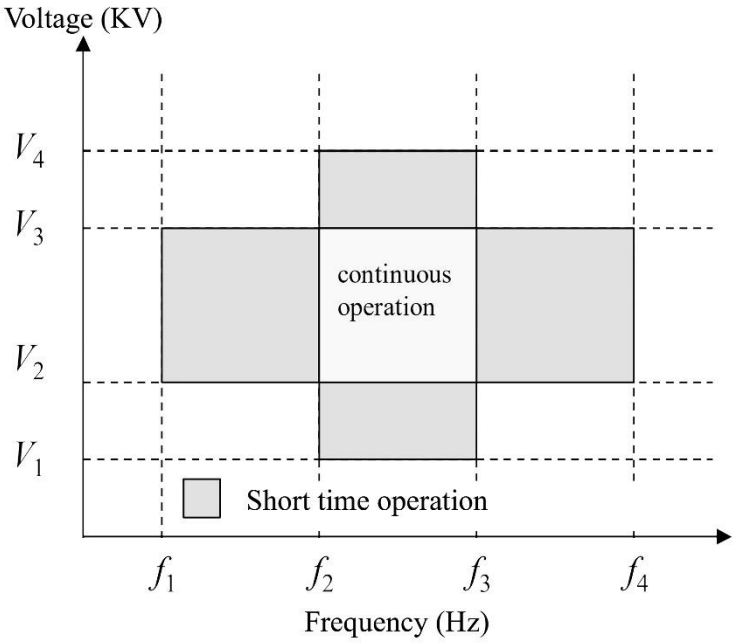

Figure 3.1: Common grid codes for operating voltage and frequency

In most present-day grid codes, WPGUs are required to have fault ride-through capability, as illustrated in Figure3.2.

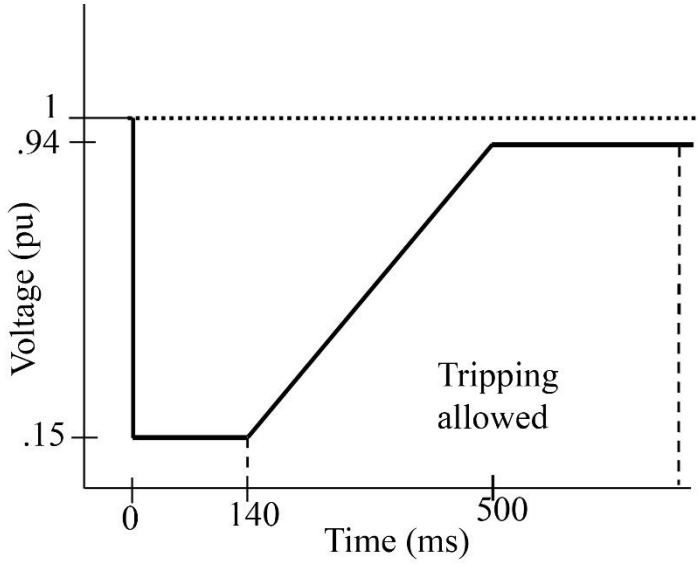

Figure 3.2: Voltage tolerance level

3.3 Power extraction from the wind

If a wind front with speed v_0 passes along a wind turbine of cross-section area A and with the air density, the turbine's output power, P_T, is calculated as follows:

$$P_T = \frac{1}{2} C_P A \rho v_0^3$$

Where, C_P is the power coefficient factor. $C_P = 4a(1-a)^2$, where, a is the perturbation factor in Betz model. Theoretically, the maximum value of $C_P = \frac{16}{27} = 0.59$, when $a = \frac{1}{3}$

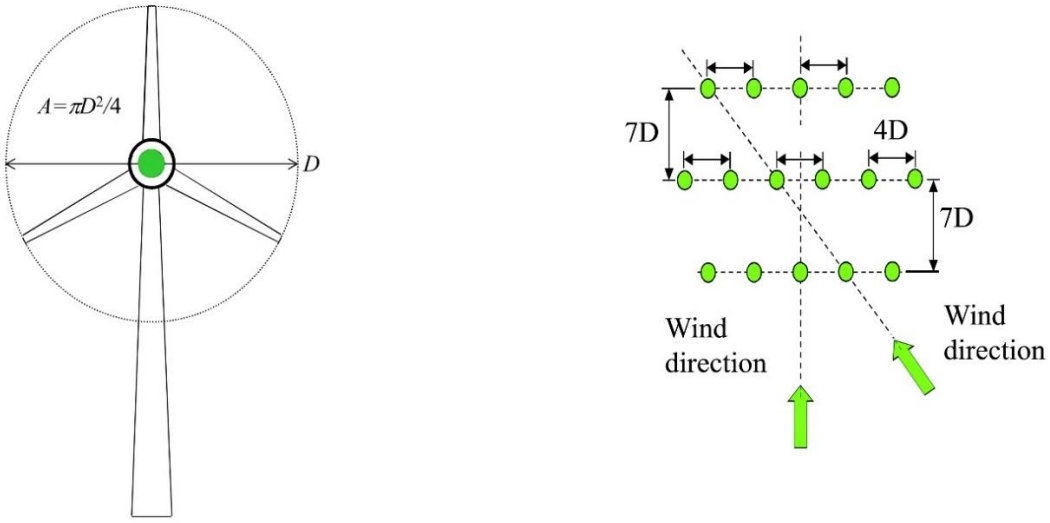

Figure 3.3 : Wind turbine and staggered arrangements of turbines

Today's commercial wind turbine have maximum power coefficients C_P of 0.45. The relationship between power coefficient and wind speed is shown in figure 3.4.

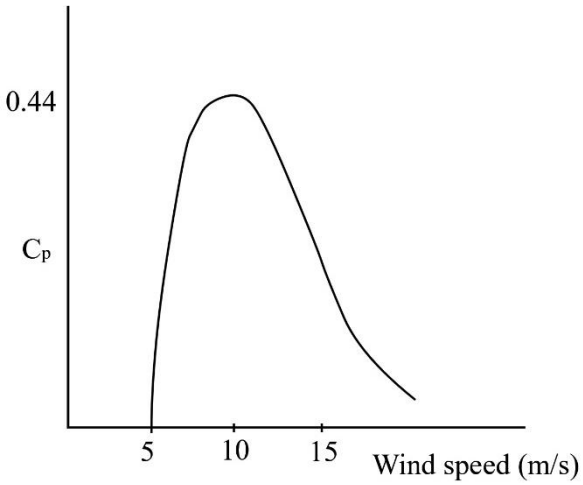

Figure 3.4 : Power coefficient and wind speed

Wind turbines operate within a certain wind speed range. The minimum wind speed at which turbine generates power is called cut-in speed (V_{ci}) and the cut-off speed (V_{co}) is the maximum allowable wind speed for the turbine's blades to keep rotating. The rated power P_R is reached at a wind speed (V_R), termed the rated wind speed. These parameters are shown in Figure 3.5.

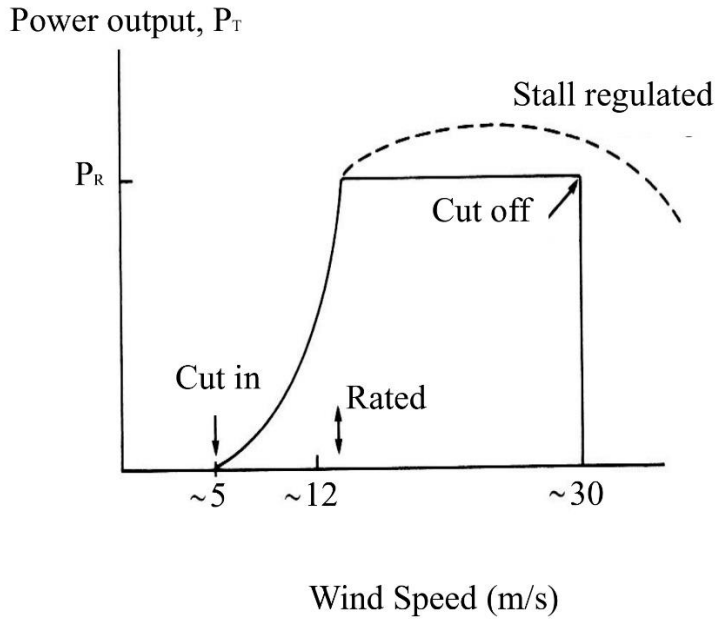

Figure 3.5 : Power curve for a typical wind turbine

The power output of a turbine could also be expressed using the cut-in and the rated wind speed and rated power.

$$P_T = a\, V_w^3 - b\, P_R$$

Where, coefficient $b = \frac{1}{\left(\frac{V_R}{V_{ci}}\right)^3 - 1}$ and coefficient $a = \frac{bP_R}{{V_{ci}}^3}$

Within a wind farm, individual turbines do not necessarily produce equal amount of power, as the wind speed reaching each turbine varies according to the turbine's orientation and spacing between turbines. Because of the array loss, the speed of the wind front reaching the m-th turbine will be:

$$V_{wm} = V_w.\left[1 - \left(1 - \sqrt{1 - C_F}\right)\left(\frac{D}{D + 2\kappa \times d_2}\right)^2\right]^{m-1}$$

V_w =avarage wind speed without array loss

C_F = turbine axial force coefficient, realistic value of $C_F = \frac{8}{9}$

$D =$ diameter of the rotor

$d =$ distance between m-th turbine and subsequence upstream turbine which causes array losses.

$m =$ positive integer number. For the first row, $m = 1$.

$\kappa =$ wake decay coefficient which can be determined by

$$\kappa = \frac{\alpha}{\log\left(\frac{h}{z_0}\right)}$$

Where, h is the turbine hub hight and z_0 is the roughness length

3.4 Turbine types

To harness wind energy in the most efficient way possible, modern wind power generators have three blades. Based on rotor speed controlling technique, turbines can be classified into fixed-speed wind turbine and variable-speed wind turbine.

3.4.1 Fixed-speed wind turbines

The turbine is equipped with a three-bladed rotor, a gearbox and an induction generator (e.g. squirrel cage induction machine) and directly connected to the power grid through a transformer. The SCIG's characteristics are: low cost, less maintenance requirements, good speed regulation, fewer power losses, better heat regulation, lightweight and compact size.

Nevertheless, SCIGs exhibit poor frequency stability and fault ride-through capability [39]. Addition to this, FSWTs are prone to produce flicker emissions. SVCs and STATCOMs may be used to increase SCIG's LVRT capabilities. Normally, fixed capacitor banks are used to provide the reactive power required for fluxing the SCIG's air-gap [40]. Power controllability is limited to changing the pitch angle.

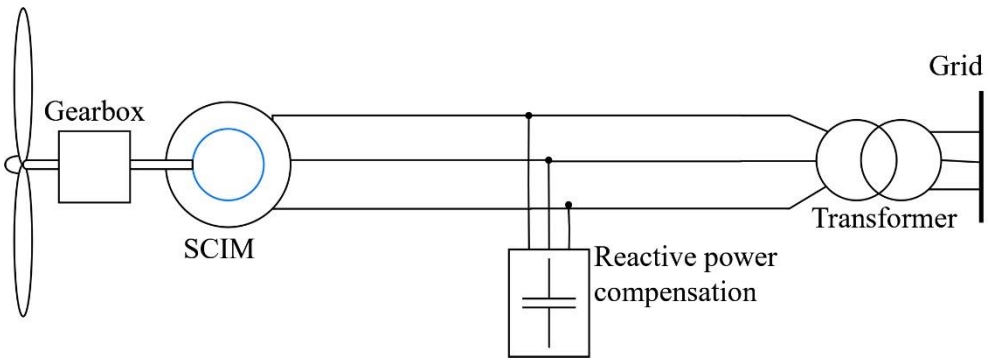

Figure 3.6: Fixed speed wind generator scheme

3.4.2 Variable speed wind turbines

Variable speed wind turbines possess great operational flexibility, which make them fully compliant with modern grid code requirements and capable of achieving maximum aerodynamic efficiencies at fluctuating wind speeds. However, harmonics and inter-harmonics are the major concerning issue with VSWTs. Doubly-feed induction generator (DFIG) and fully-rated converter wind power generators are the most noteworthy turbines in this category.

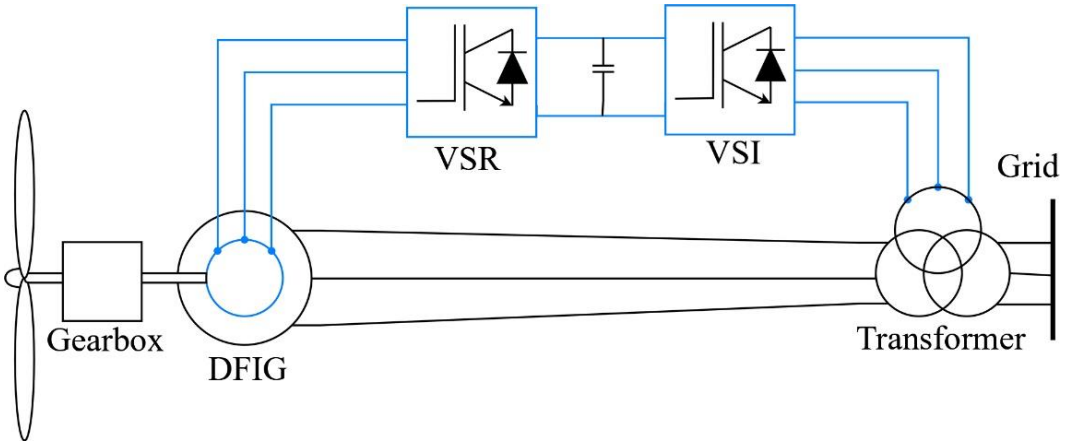

Figure 3.7: DFIG wind turbine scheme.

Figure 3.7 illustrates a typical schematic circuit of a DFIG. Basically, the stator winding of a wound rotor induction generator with slip rings, is coupled with the power grid through a connecting transformer and a small back-to-back VSC-HVDC links the rotor winding with the power grid. To such an end, the rotor's slip rings and the tertiary winding of the power transformer are used, respectively. The power converters manipulate the rotor voltage so that generator operates over a large speed range (40%) [41]. When the slip is negative, the generator operates above synchronous speed and the rotor and the stator circuits feed power to the grid. In case of rotor speed below synchronous speed, the rotor consumes power from the grid and only the stator circuit delivers power to the grid.

In wind turbine schemes with fully-rated converters, either a permanent magnet synchronous generator or a squirrel cage induction generator is connected to the power grid through fully rated VSR and VSI connected back-to-back. This power electronic arrangement decouples frequency-wise the wind power generator from the power grid; hence independent speed-control of the turbine is achieved over a wide range speed. The schematic diagram of a SCIG with fully rated converter is shown in Figure 3.8, where the reactive power compensation to flux the generator is provided by VSR. As SCIG needs

gearbox, power losses of the overall system is one of its main drawbacks since in addition to the gearbox, power losses are also incurred by the generator and the two VSCs.

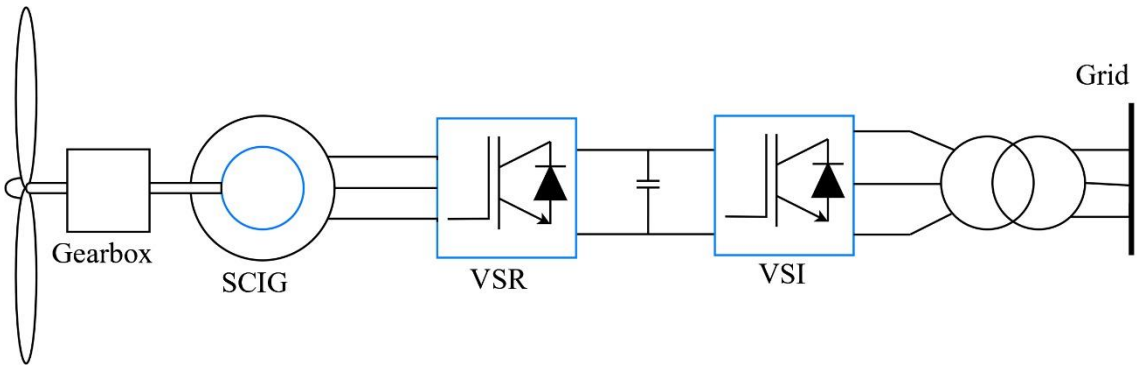

Figure 3.8: SCIG wind turbine with fully rated converter

The schematic representation of a PMSG is shown in Figure 3.9. This is a rapidly expanding option in wind power generation, particularly in the multi-MW range intended for offshore wind farms. As permanent magnets are used instead of field copper windings, it yields higher power densities. It produces sinusoidal back emf with under-excited field excitation. The gearbox can be excluded, as PMSG runs at low synchronous speeds.

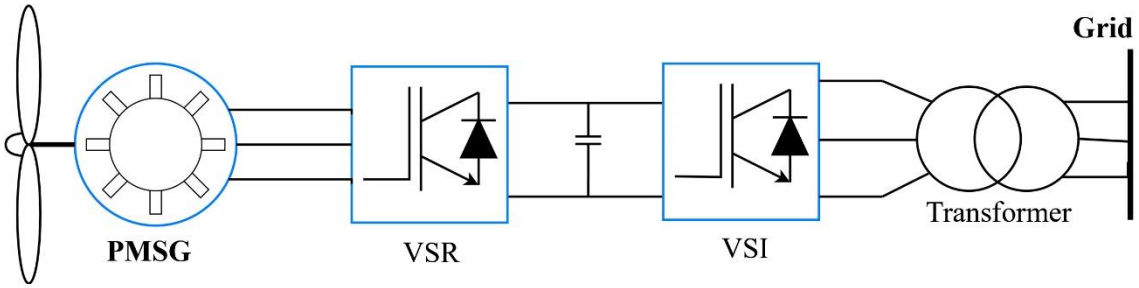

Figure 3.9: PMSG wind turbine with fully rated converter.

3.5 Conclusion

The stochastic characteristics of wind power and the effect of installation in medium voltage distribution networks were discussed. Overloading, overvoltage, frequency fluctuations, harmonics and flicker are the main limiting factors to connect a wind farm in low-voltage distribution system networks. The smooth integration of wind farms may need appropriate use of AC-DC-AC links to overcome these issues. The SCIG and the PMSG wind turbines are the example wind power technologies used in this thesis to study voltage and active and reactive powers control issues in grid-connected wind farms through VSC-HVDC links.

4. POWER FLOWS: BACK-TO-BACK VSC-HVDC FOR THE GRID CONNECTION OF WIND FARMS

Power flow studies are an essential tool in power systems to ensure that voltage magnitudes and phase angles, the flow of active and reactive powers and the power losses of the power network are all within acceptable boundaries. To carry out efficient power flow studies, large sets of nonlinear algebraic equations must be solved in a fast and reliable way. In this thesis, the well-known Newton-Raphson(N-R) iterative method is used because of its fast-convergence capability and robustness towards the solution. The chapter deals with developing mathematical models for VSC-HVDCs, SGIGs and PMSGs equipment suitable for incorporation into a generic N-R power flow algorithm.

4.1 Newton-Raphson power flow solution

The Newton-Raphson method is iterative in nature and as such, in the first step of N-R power flow algorithm, all state variables need to be given suitable initial values and all network parameters data must be supplied correctly to carry out accurate calculations. In the next step, power mismatches are calculated. If the results are not within pre-specified bounds, the Jacobian elements are evaluated and the linearized set of power-voltage equations are solved to update the nodal voltage values. The process continues until all power mismatches becomes smaller than a pre-specified tolerance value.

4.2 Bus-types

Three types of buses are defined in conventional power flow study based on whether the values of active power, reactive power, voltage magnitude and voltage phase-angle are known a priori or not.

Types of buses	Known value	Computed value
Generator bus (PV)	Voltage magnitude and active power	Voltage angle and reactive power
Slack or swing	Voltage magnitude and angle	Active and reactive power
Load (PQ)	Active and reactive power	Voltage magnitude and angle

4.3 PMSG model in the power flow algorithm

The positive sequence equivalent circuit and phasor diagram of a PMSG are illustrated below.

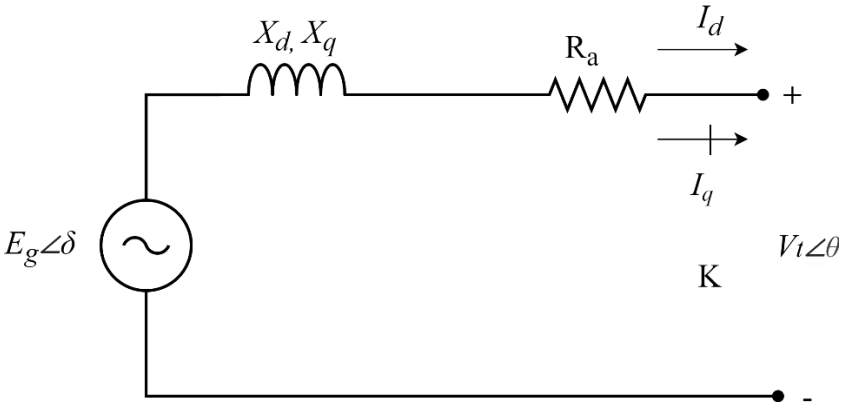

Figure 4.1: Positive sequence equivalent circuit of PMSG.

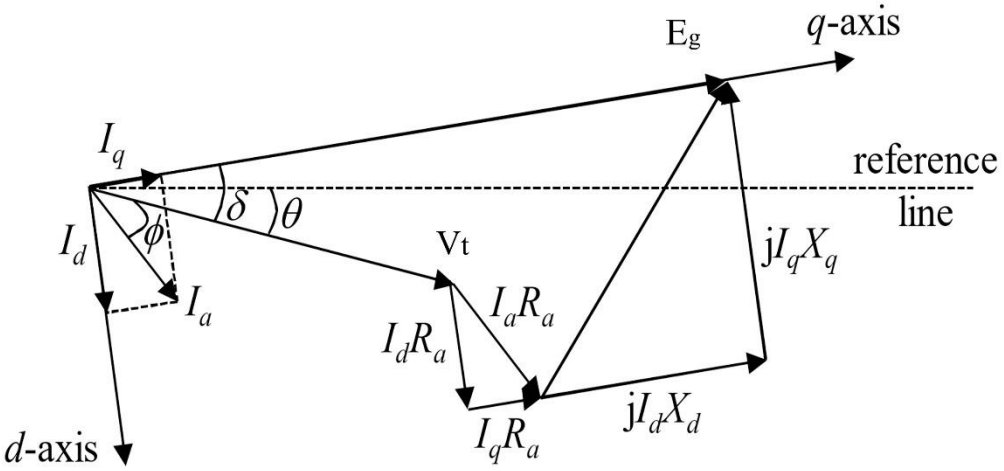

Figure 4.2: Phasor diagram of PMSG

Where,

$$\overline{E_g} = \bar{V}_t + j\,X_d I_d + j\,X_q I_q + R_a \bar{I}_a \tag{5.1}$$

$$\begin{bmatrix} E_d \\ E_q \end{bmatrix} = \begin{bmatrix} V_d \\ V_q \end{bmatrix} + \begin{bmatrix} R_a & -X_q \\ X_d & R_a \end{bmatrix} \begin{bmatrix} I_d \\ I_q \end{bmatrix} \tag{5.2}$$

$$\begin{bmatrix} I_d \\ I_q \end{bmatrix} = \frac{1}{\Delta} \cdot \begin{bmatrix} R_a & X_q \\ -X_d & R_a \end{bmatrix} \left\{ \begin{bmatrix} E\cos\delta \\ E\sin\delta \end{bmatrix} - \begin{bmatrix} V\cos\theta \\ V\sin\theta \end{bmatrix} \right\} \tag{5.3}$$

Here, $\Delta = R_a^2 + X_d X_q$

At the air-gap line, $$\begin{bmatrix} P_g \\ Q_g \end{bmatrix} = E_g \cdot \begin{bmatrix} \cos\delta & -\sin\delta \\ \sin\delta & \cos\delta \end{bmatrix} \begin{bmatrix} I_d \\ I_q \end{bmatrix}^* \quad (5.4)$$

At node-k, $$\begin{bmatrix} P_k \\ Q_k \end{bmatrix} = -V_t \cdot \begin{bmatrix} \cos\theta & -\sin\theta \\ \sin\theta & \cos\theta \end{bmatrix} \begin{bmatrix} I_d \\ I_q \end{bmatrix}^* \quad (5.5)$$

Developing these equations further,

$$\begin{bmatrix} P_g \\ Q_g \end{bmatrix} = \frac{E_g}{\Delta} \cdot \begin{bmatrix} \cos\delta & -\sin\delta \\ \sin\delta & \cos\delta \end{bmatrix} \begin{bmatrix} R_a & -X_q \\ X_d & R_a \end{bmatrix} \left\{ \begin{bmatrix} E_g\cos\delta \\ -E_g\sin\delta \end{bmatrix} - \begin{bmatrix} V_t\cos\theta \\ -V_t\sin\theta \end{bmatrix} \right\} \quad (5.6)$$

$$= \frac{E_g}{\Delta} \cdot \begin{bmatrix} (R_a\cos\delta - X_d\sin\delta) & (-X_q\cos\delta - R_a\sin\delta) \\ (R_a\sin\delta + X_d\cos\delta) & (-X_q\sin\delta + R_a\cos\delta) \end{bmatrix} \begin{bmatrix} E_g\cos\delta - V_t\cos\theta \\ -E_g\sin\delta + V_t\sin\theta \end{bmatrix}$$

$$= \frac{E_g}{\Delta} \cdot \begin{bmatrix} (R_a\cos\delta - X_d\sin\delta)(E_g\cos\delta - V_t\cos\theta) - (-X_q\cos\delta - R_a\sin\delta)(E_g\sin\delta - V_t\sin\theta) \\ (R_a\sin\delta + X_d\cos\delta)\big(E_g\cos\delta - V_t\cos\theta\big) - (-X_q\sin\delta + R_a\cos\delta)(E_g\sin\delta - V_t\sin\theta) \end{bmatrix}$$

$$= \frac{1}{\Delta} \cdot \begin{bmatrix} E_g^2 R_a + E_g^2\big(X_q - X_d\big)\sin\delta\cos\delta - E_g V_t R_a\cos(\delta-\theta) + E_g V_t(X_d\sin\delta\cos\theta - X_q\cos\delta\sin\theta) \\ E_g^2\big(X_d\cos^2\delta + X_q\sin^2\delta\big) - E_g V_t R_a\sin(\delta-\theta) - E_g V_t(X_d\cos\delta\cos\theta + X_q\sin\delta\sin\theta \end{bmatrix}$$

(5.7)

At the PMSG output terminal (node-K),

$$\begin{bmatrix} P_k \\ Q_k \end{bmatrix} = \frac{V_t}{\Delta} \cdot \begin{bmatrix} \cos\theta & -\sin\theta \\ \sin\theta & \cos\theta \end{bmatrix} \begin{bmatrix} R_a & -X_q \\ X_d & R_a \end{bmatrix} \left\{ \begin{bmatrix} V_t\cos\theta \\ -V_t\sin\theta \end{bmatrix} - \begin{bmatrix} E_g\cos\delta \\ -E_g\sin\delta \end{bmatrix} \right\} \quad (5.8)$$

$$= \frac{V_t}{\Delta} \cdot \begin{bmatrix} (R_a\cos\theta - X_d\sin\theta) & (-X_q\cos\theta - R_a\sin\theta) \\ (R_a\sin\theta + X_d\cos\theta) & (-X_q\sin\theta + R_a\cos\theta) \end{bmatrix} \begin{bmatrix} V_t\cos\theta - E_g\cos\delta \\ -V_t\sin\theta + E_g\sin\delta \end{bmatrix}$$

$$= \frac{V_t}{\Delta} \cdot \begin{bmatrix} (R_a\cos\theta - X_d\sin\theta)(V_t\cos\theta - E_g\cos\delta) - (-X_q\cos\theta - R_a\sin\theta)(V_t\sin\theta - E_g\sin\delta) \\ (R_a\sin\theta + X_d\cos\theta)\big(V_t\cos\theta - E_g\cos\delta\big) - (-X_q\sin\theta + R_a\cos\theta)(V_t\sin\theta - E_g\sin\delta) \end{bmatrix}$$

$$= \frac{1}{\Delta} \cdot \begin{bmatrix} V_t^2 R_a + V_t^2\big(X_q - X_d\big)\sin\theta\cos\theta - V_t E_g R_a\cos(\theta-\delta) + V_t E_g(X_d\sin\theta\cos\delta - X_q\cos\theta\sin\delta) \\ V_t^2\big(X_d\cos^2\theta + X_q\sin^2\theta\big) - V_t E_g R_a\sin(\theta-\delta) - V_t E_g(X_d\cos\theta\cos\delta + X_q\sin\theta\sin\delta \end{bmatrix}$$

(5.9)

To perform the iterative solution using the Newton-Raphson method, the linearized equations are shown below in matrix form, which represent the relationship between changes in active and reactive powers and changes in nodal voltage magnitudes and phase angles.

$$\begin{bmatrix} \Delta P_k \\ \Delta Q_k \\ \Delta P_g \\ \Delta Q_g \end{bmatrix} = \begin{bmatrix} \partial\Delta P_k/\partial\theta_k & (\partial\Delta P_k/\partial V_k)/V_k & \partial\Delta P_k/\partial\delta & (\partial\Delta P_k/\partial E_g)/E_g \\ \partial\Delta Q_k/\partial\theta_k & (\partial\Delta Q_k/\partial V_k)/V_k & \partial\Delta Q_k/\partial\delta & (\partial\Delta Q_k/\partial E_g)/E_g \\ \partial\Delta P_g/\partial\theta_k & (\partial\Delta P_g/\partial V_k)/V_k & \partial\Delta P_g/\partial\delta & (\partial\Delta P_g/\partial E_g)/E_g \\ \partial\Delta Q_g/\partial\theta_k & (\partial\Delta Q_g/\partial V_k)/V_k & \partial\Delta Q_g/\partial\delta & (\partial\Delta Q_g/\partial E_g)/E_g \end{bmatrix} \begin{bmatrix} \Delta\theta_k \\ \Delta V_k/V_k \\ \Delta\delta \\ \Delta E_g/E_g \end{bmatrix} \quad (5.10)$$

The self-Jacobian elements at node-K are:

$$\frac{\partial \Delta P_k}{\partial \theta_k} = -\left(-Q_k - V_k^2 B_{kk}\right); \quad \left(\frac{\partial \Delta P_k}{\partial V_k}\right).V_k = -\left(P_k + V_k^2 G_{kk}\right) \tag{5.11}$$

$$\frac{\partial \Delta Q_k}{\partial \theta_k} = -\left(P_k - V_k^2 G_{kk}\right); \quad \left(\frac{\partial \Delta Q_k}{\partial V_k}\right).V_k = -\left(Q_k - V_k^2 B_{kk}\right) \tag{5.12}$$

The mutual Jacobian elements between node-K and the air-gap line, are:

$$\begin{aligned}
\frac{\partial \Delta P_k}{\partial \delta} &= -\left(V_k E_g\left\{G_{kg}\sin(\theta_k - \delta) - B_{kg}\cos(\theta_k - \delta)\right\}\right) \\
\frac{\partial \Delta P_k}{\partial E_g}.E_g &= -\left(V_k E_g\left\{G_{kg}\cos(\theta_k - \delta) + B_{kg}\sin(\theta_k - \delta)\right\}\right) \\
\frac{\partial \Delta Q_k}{\partial \delta} &= -\left(-V_k E_g\left\{G_{kg}\cos(\theta_k - \delta) + B_{kg}\sin(\theta_k - \delta)\right\}\right) \\
\frac{\partial \Delta Q_k}{\partial E_g}.E_g &= -\left(V_k E_g\left\{G_{kg}\sin(\theta_k - \delta) - B_{kg}\cos(\theta_k - \delta)\right\}\right)
\end{aligned} \tag{5.13}$$

The self-Jacobian elements at the air-gap line are:

$$\frac{\partial \Delta P_g}{\partial \delta} = -\left(-Q_g - E_g^2 B_{gg}\right); \quad \left(\frac{\partial \Delta P_g}{\partial E_g}\right).E_g = -\left(P_g + E_g^2 B_{gg}\right) \tag{5.14}$$

$$\frac{\partial \Delta Q_g}{\partial \delta} = -\left(P_g - E_g^2 B_{gg}\right); \quad \left(\frac{\partial \Delta Q_g}{\partial E_g}\right).E_g = -\left(Q_g - E_g^2 B_{gg}\right) \tag{5.15}$$

The mutual elements between the air-gap line and node K, are:

$$\begin{aligned}
\frac{\partial \Delta P_g}{\partial \theta_k} &= -\left(E_g V_k\left\{G_{gk}\sin(\delta - \theta_k) - B_{gk}\cos(\delta - \theta_k)\right\}\right) \\
\frac{\partial \Delta P_g}{\partial V_k}.V_k &= -\left(E_g V_k\left\{G_{gk}\cos(\delta - \theta_k) + B_{gk}\sin(\delta - \theta_k)\right\}\right) \\
\frac{\partial \Delta Q_g}{\partial \theta_k} &= -\left(-E_g V_k\left\{G_{gk}\cos(\delta - \theta_k) + B_{gk}\sin(\delta - \theta_k)\right\}\right) \\
\frac{\partial \Delta Q_g}{\partial V_k}.V_k &= -\left(E_g V_k\left\{G_{gk}\sin(\delta - \theta_k) - B_{gk}\cos(\delta - \theta_k)\right\}\right)
\end{aligned} \tag{5.16}$$

The power mismatches for node K and the air-gap line, are:

$$\begin{aligned}
\Delta P_k &= P_k^{net} - (P_{grid}^{cal} + P_k^{cal}) \\
\Delta Q_k &= Q_k^{net} - (Q_{grid}^{cal} + Q_k^{cal}) \\
\Delta P_g &= -P_g^{cal} \\
\Delta Q_g &= -Q_g^{cal}
\end{aligned} \tag{5.17}$$

4.4 SCIG model in the power flow algorithm

The positive sequence equivalent circuit of the SCIM is illustrated in Figure 5.3. This is used as the basis for developing the power equations of the SCIM.

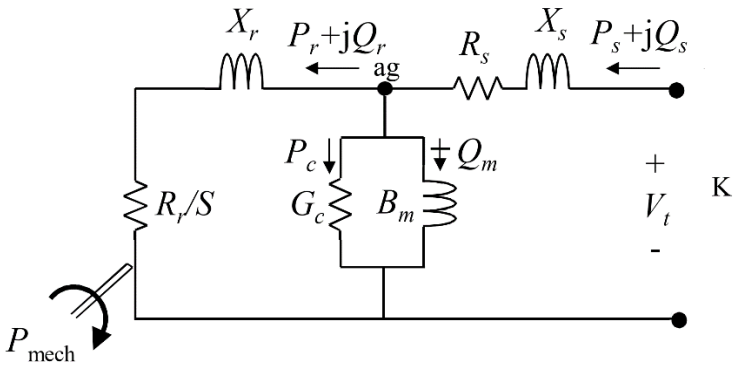

Figure 4.3 : Positive sequence equivalent circuit of SCIM.

The complex power at the network end (node K) is defined by the following equations.

$$\bar{S}_k = \bar{Y}_{eq}^{*} V_t^2$$

$$\bar{S}_k = \left(\frac{R_{eq}}{R_{eq}^2+X_{eq}^2} + j\frac{X_{eq}}{R_{eq}^2+X_{eq}^2}\right)V_t^2 \tag{5.18}$$

$$\begin{bmatrix} P_k \\ Q_k \end{bmatrix} = \begin{bmatrix} \frac{R_{eq}}{R_{eq}^2+X_{eq}^2} V_t^2 \\ \frac{X_{eq}}{R_{eq}^2+X_{eq}^2} V_t^2 \end{bmatrix} \tag{5.19}$$

Where,

$$R_{eq} = R_s + \frac{\left(G_c + \frac{SR_r}{R_r^2+S^2X_r^2}\right)}{\left(G_c + \frac{SR_r}{R_r^2+S^2X_r^2}\right)^2 + \left(B_m - \frac{S^2X_r}{R_r^2+S^2X_r^2}\right)^2}$$

$$\mathrm{X}_{eq} = \mathrm{X}_s + \frac{\left(B_m - \frac{S^2\mathrm{X}_r}{R_r^2+S^2X_r^2}\right)}{\left(G_c + \frac{SR_r}{R_r^2+S^2X_r^2}\right)^2 + \left(B_m - \frac{S^2\mathrm{X}_r}{R_r^2+S^2X_r^2}\right)^2}$$

At the rotor end the following equation are relevant,

$$P_{mech} = (1-S)P_r \tag{5.20}$$

The rotor power, is,

$$\begin{bmatrix} P_r \\ Q_r \end{bmatrix} = \begin{bmatrix} G_r V_{ag}^2 \\ -B_r V_{ag}^2 \end{bmatrix} \tag{5.21}$$

where $G_r = \frac{SR_r}{R_r^2 + S^2 X_r^2}$ and $B_r = -\frac{S^2 X_r}{R_r^2 + S^2 X_r^2}$

The nodal currents are:

$$\begin{bmatrix} \bar{I}_s \\ \bar{I}_{ag} \end{bmatrix} = \begin{bmatrix} \bar{Y}_s & -\bar{Y}_s \\ -\bar{Y}_s & \bar{Y}_s + \bar{Y}_m \end{bmatrix} \begin{bmatrix} \bar{V}_s \\ \bar{V}_{ag} \end{bmatrix} \tag{5.22}$$

Where, $\bar{Y}_s = \frac{R_s}{R_s^2 + X_s^2} - j\,\frac{X_s}{R_s^2 + X_s^2}$ and $\bar{Y}_m = G_c + jB_m$

The stator and air-gap complex power equations are:

$$\begin{bmatrix} \bar{S}_s \\ \bar{S}_{ag} \end{bmatrix} = \begin{bmatrix} \bar{V}_s & 0 \\ 0 & \bar{V}_{ag} \end{bmatrix} \begin{bmatrix} \bar{I}_s \\ \bar{I}_{ag} \end{bmatrix}^*$$

$$= \begin{bmatrix} \bar{Y}_s^* V_s^2 - \bar{Y}_s^* \bar{V}_s \bar{V}_{ag}^* \\ -\bar{Y}_s^* \bar{V}_{ag} \bar{V}_s^* + (\bar{Y}_s^* + \bar{Y}_m^*) V_{ag}^2 \end{bmatrix} \tag{5.23}$$

Where, $\bar{V}_s = V_s(cos\theta_s + jsin\theta_s)$

$\bar{V}_{ag} = V_{ag}(cos\theta_{ag} + jsin\theta_{ag})$

Developing the (5.23) further,

Stator power:

$$P_s = G_s V_s^2 - V_s V_{ag}\{G_s \cos(\theta_s - \theta_{ag}) + B_s \sin(\theta_s - \theta_{ag})\}$$

$$Q_s = -B_s V_s^2 - V_s V_{ag}\{G_s \sin(\theta_s - \theta_{ag}) - B_s \cos(\theta_s - \theta_{ag})\} \tag{5.24}$$

Power at the air-gap line:

$$P_{ag} = (G_s + G_c) V_{ag}^2 - V_s V_{ag}\{G_s \cos(\theta_{ag} - \theta_s) + B_s \sin(\theta_{ag} - \theta_s)\}$$

$$Q_{ag} = -(B_s + B_m) V_{ag}^2 - V_s V_{ag}\{G_s \sin(\theta_{ag} - \theta_s) - B_s \cos(\theta_{ag} - \theta_s)\} \tag{5.25}$$

Equations (5.24) and (5.25) are used to develop the linearized equations with which to perform the power flow study.

4.5 Back-to-back, VSC-HVDC model in the power flow algorithm

The equivalent circuit of a two-level, back-to-back HVDC link is shown in Figure 5.2. DC side of both inverter and rectifiers are sharing a common bus.

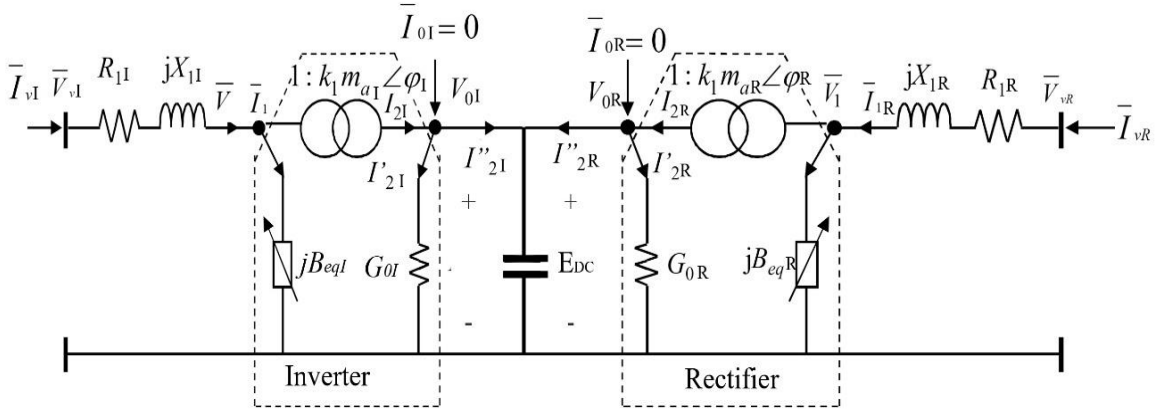

Figure 4.4: Equivalent circuit of back-to-back VSC-HVDC link

At the rectifier side, $\bar{V}_{1R} = k_1 m_a e^{j\varphi} E_{DC}$ (5.26)

$$V_{oR} I_{2R} = Re(\overline{V_{1R}}\ \bar{I}^*_{1R}))$$

$$V_{oR} I_{2R} = \overline{V_{1R}}\ (\bar{I}^*_{1R} - \bar{I}'^*_{oR}) = \overline{V_{1R}}\ \bar{I}^*_{1R} + jB_{eqR} V^2_{1R} \quad (5.27)$$

$$G_{oR} = \left(\frac{I^{nom}_{2R}}{I^{act}_{2R}}\right)^2 = G_{sw}$$

$$\begin{pmatrix} \bar{I}_{vR} \\ \bar{I}_{oR=0} \end{pmatrix} = \begin{pmatrix} \bar{Y}_{1R} & -K_1 m_{aR}(cos\varphi_R + jsin\varphi_R)\bar{Y}_{1R} \\ -K_1 m_{aR}(cos\varphi_R - jsin\varphi_R)\bar{Y}_{1R} & G_{sw} + k_1^2 m_{aR}^2(\bar{Y}_{1R} + jB_{eqR}) \end{pmatrix} \begin{pmatrix} \bar{V}_{vR} \\ V_{oR} \end{pmatrix} \quad (5.28)$$

The complex power equations are,

$$\begin{pmatrix} \bar{S}_{vR} \\ \bar{S}_{oR} \end{pmatrix} = \begin{pmatrix} \bar{V}_{vR} & 0 \\ 0 & V_{oR} \end{pmatrix} \begin{pmatrix} \bar{I}^*_{vR} \\ \bar{I}^*_{oR} \end{pmatrix}$$

$$\begin{pmatrix} \bar{S}_{vR} \\ \bar{S}_{oR} \end{pmatrix} = \begin{pmatrix} \bar{V}_{vR} & 0 \\ 0 & V_{oR} \end{pmatrix} \left\{ \begin{pmatrix} \overline{Y^*}_{1R} & -K_1 m_{aR}(cos\varphi_R + jsin\varphi_R)\overline{Y^*}_{1R} \\ -K_1 m_{aR}(cos\varphi_R - jsin\varphi_R)\overline{Y^*}_{1R} & G_{sw} + k_1^2 m_{aR}^2(\overline{Y^*}_{1R} + jB_{eqR}) \end{pmatrix} \begin{pmatrix} \overline{V^*}_{vR} \\ V_{oR} \end{pmatrix} \right\} \quad (5.29)$$

Developing equation further, the active and reactive power equations of the rectifier are:

$$P_{vR} = G_{1R} V^2_{vR} - K_1 m_{aR} V_{vR} V_{oR} [G_{1R} \cos(\theta_{vR} - \theta_{oR} - \varphi_R) + B_{1R} \sin(\theta_{vR} - \theta_{oR} - \varphi_R)]$$

$$Q_{vR} = -B_{1R} V^2_{vR} - K_1 m_{aR} V_{vR} V_{oR} [G_{1R} \sin(\theta_{vR} - \theta_{oR} - \varphi_R) - B_{1R} \cos(\theta_{vR} - \theta_{oR} - \varphi_R)]$$

$$P_{oR} = (K_1^2 m_{aR}^2 G_{1R} + G_{swR}) V_{oR}^2 - K_1 m_{aR} V_{vR} V_{oR} [G_{1R} \cos(\theta_{oR} - \theta_{vR} + \varphi_R) + B_{1R} \sin(\theta_{oR} - \theta_{vR} + \varphi_R)]$$
$$Q_{oR} = -K_1^2 m_{aR}^2 (B_{1R} + B_{eqR}) V_{oR}^2 - K_1 m_{aR} V_{vR} V_{oR} [G_{1R} \sin(\theta_{oR} - \theta_{vR} + \varphi_R) - B_{1R} \cos(\theta_{oR} - \theta_{vR} + \varphi_R)] \quad (5.30)$$

Likewise, the nodal power equations for the inverter are:

$$P_{vI} = G_{1I} V_{vI}^2 - K_1 m_{aI} V_{vI} V_{oI} [G_{1I} \cos(\theta_{vI} - \theta_{oI} - \varphi_I) + B_{1I} \sin(\theta_{vI} - \theta_{oI} - \varphi_I)]$$
$$Q_{vI} = -B_{1I} V_{vI}^2 - K_1 m_{aI} V_{vI} V_{oI} [G_{1I} \sin(\theta_{vI} - \theta_{oI} - \varphi_I) - B_{1I} \cos(\theta_{vI} - \theta_{oI} - \varphi_I)]$$
$$P_{oI} = (K_1^2 m_{aI}^2 G_{1I} + G_{swI}) V_{oI}^2 - K_1 m_{aI} V_{vI} V_{oI} [G_{1I} \cos(\theta_{oI} - \theta_{vI} + \varphi_I) + B_{1I} \sin(\theta_{oI} - \theta_{vI} + \varphi_I)]$$
$$Q_{oI} = -K_1^2 m_{aI}^2 (B_{1I} + B_{eqI}) V_{oI}^2 - K_1 m_{aI} V_{vI} V_{oI} [G_{1I} \sin(\theta_{oI} - \theta_{vI} + \varphi_I) - B_{1I} \cos(\theta_{oI} - \theta_{vI} + \varphi_I)] \quad (5.31)$$

Equations (5.30) and (5.31) are used to determine the calculated active and reactive powers. The mismatch power terms are calculated using the following equations,

$$\Delta P_{vR} = (P_{vR,gen} - P_{vR,load}) - P_{vR,cal}$$
$$\Delta Q_{vR} = (Q_{vR,gen} - Q_{vR,load}) - Q_{vR,cal}$$
$$\Delta P_{vI} = (P_{vI,gen} - P_{vI,load}) - P_{vI,cal}$$
$$\Delta Q_{vI} = (Q_{vI,gen} - Q_{vI,load}) - Q_{vI,cal}$$
$$\Delta P_{oR} = (P_{oR,gen} - P_{oR,load}) - P_{oR,cal}$$
$$\Delta Q_{oR} = (Q_{oR,gen} - Q_{oR,load}) - Q_{oR,cal}$$
$$\Delta P_{oR-vR} = P_{oR-vR,reg} - P_{oR-vR,cal}$$
$$\Delta Q_{oR-vR} = o - Q_{oR-vR,cal}$$
$$\Delta P_{oI} = (P_{oI,gen} - P_{oI,load}) - P_{oI,cal}$$
$$\Delta Q_{oI} = (Q_{oI,gen} - Q_{oI,load}) - Q_{oI,cal}$$
$$\Delta P_{oI-vI} = P_{oI-vI,reg} - P_{oI-vI,cal}$$
$$\Delta Q_{oI-vI} = o - Q_{oI-vI,cal} \quad (5.32)$$

To perform the iterative solution using the Newton-Raphson method, the linearized equations (5.33) are used. This matrix equation represents the relationship between changes in active and reactive powers and changes in nodal voltage magnitudes and phase angles. It is a common practice that power at the DC side is regulated by the rectifier and the voltage at the AC side is regulated by the inverter. Power regulation is done by using: $\theta_{vR}, V_{vR}, \theta_{vI}, m_{aI}, \theta_0, V_{vI}, \varphi_R, B_{eqR}, \varphi_I$ and B_{eqI}. Voltage regulation is done by using: m_{aI}.

$$
\begin{bmatrix}
\Delta P_{vR} \\
\Delta Q_{vR} \\
\Delta P_{vI} \\
\Delta Q_{vI} \\
\Delta P_{oR} + \Delta P_{oI} \\
\Delta Q_{oR} + \Delta Q_{oI} \\
\Delta P_{oR-vR} \\
\Delta Q_{oR-vR} \\
\Delta P_{oI-vI} \\
\Delta Q_{oI-vI}
\end{bmatrix} =
$$

$$
\begin{bmatrix}
\frac{\partial P_{vR}}{\partial \theta_{vR}} & \frac{\partial P_{vR}}{\partial V_{vR}} V_{vR} & 0 & 0 & \frac{\partial P_{vR}}{\partial \theta_0} & 0 & \frac{\partial P_{vR}}{\partial \varphi_R} & \frac{\partial P_{vR}}{\partial B_{eqR}} & 0 & 0 \\
\frac{\partial Q_{vR}}{\partial \theta_{vR}} & \frac{\partial Q_{vR}}{\partial V_{vR}} V_{vR} & 0 & 0 & \frac{\partial Q_{vR}}{\partial \theta_0} & 0 & \frac{\partial Q_{vR}}{\partial \varphi_R} & \frac{\partial Q_{vR}}{\partial B_{eqR}} & 0 & 0 \\
0 & 0 & \frac{\partial P_{vI}}{\partial \theta_{vI}} & \frac{\partial P_{vR}}{\partial m_{aI}} m_{aI} & 0 & 0 & 0 & 0 & \frac{\partial P_{vI}}{\partial \varphi_I} & \frac{\partial P_{vI}}{\partial B_{eqI}} \\
0 & 0 & \frac{\partial Q_{vI}}{\partial \theta_{vI}} & \frac{\partial Q_{vR}}{\partial m_{aI}} m_{aI} & 0 & 0 & 0 & 0 & \frac{\partial Q_{vI}}{\partial \varphi_I} & \frac{\partial Q_{vI}}{\partial B_{eqI}} \\
\frac{\partial P_{oR}}{\partial \theta_{vR}} & \frac{\partial P_{oR}}{\partial V_{vR}} V_{vR} & \frac{\partial P_{oI}}{\partial \theta_{vI}} & \frac{\partial P_{oI}}{\partial m_{aI}} m_{aI} & \frac{\partial P_{oR}}{\partial \theta_0} & 0 & \frac{\partial P_{oR}}{\partial \varphi_R} & \frac{\partial P_{oR}}{\partial B_{eqR}} & \frac{\partial P_{oI}}{\partial \varphi_I} & \frac{\partial P_{oI}}{\partial Beq_I} \\
0 & 0 & 0 & 0 & 0 & 1 & 0 & 0 & 0 & 0 \\
\frac{\partial P_{oR-vR}}{\partial \theta_{vR}} & \frac{\partial P_{oR-vR}}{\partial V_{vR}} V_{vR} & 0 & 0 & \frac{\partial P_{oR-vR}}{\partial \theta_0} & 0 & \frac{\partial P_{oR-vR}}{\partial \varphi_R} & \frac{\partial P_{oR}-vR}{\partial B_{eqR}} & 0 & 0 \\
\frac{\partial Q_{oR-vR}}{\partial \theta_{vR}} & \frac{\partial Q_{oR-vR}}{\partial V_{vR}} V_{vR} & 0 & 0 & \frac{\partial Q_{oR-vR}}{\partial \theta_0} & 0 & \frac{\partial Q_{oR-vR}}{\partial \varphi_R} & \frac{\partial Q_{oR-vR}}{\partial B_{eqR}} & 0 & 0 \\
0 & 0 & \frac{\partial P_{oI-vI}}{\partial \theta_{vI}} & \frac{\partial P_{oI-vI}}{\partial m_{aI}} m_{aI} & 0 & 0 & 0 & 0 & \frac{\partial P_{oI-vI}}{\partial \varphi_I} & \frac{\partial P_{oI-vI}}{\partial Beq_I} \\
0 & 0 & \frac{\partial Q_{oI-vI}}{\partial \theta_{vI}} & \frac{\partial Q_{oI-vI}}{\partial m_{aI}} m_{aI} & 0 & 0 & 0 & 0 & \frac{\partial Q_{oI-vI}}{\partial \varphi_I} & \frac{\partial Q_{oI-vI}}{\partial B_{eqI}}
\end{bmatrix} \times
$$

$$
\begin{bmatrix}
\Delta \theta_{vR} \\
\Delta V_{vR}/V_{vR} \\
\Delta \theta_{vI} \\
\Delta m_{aI}/m_{aI} \\
\Delta \theta_0 \\
\Delta V_{vI}/V_{vI} \\
\Delta \varphi_R \\
\Delta B_{eqR} \\
\Delta \varphi_I \\
\Delta B_{eqI}
\end{bmatrix} \tag{5.33}
$$

4.6 Conclusion

The detailed mathematical model of the back-to-back, VSC-HVDC link, the PMSG and the SCIG are introduced in this chapter for the purpose of carrying out power flow studies. The active power generated by the wind farm is regulated by the VSC-HVDC link's rectifier by suitable adjustment of the state variables. The VSC-HVDC link's inverter offers degree of freedom to regulate nodal voltage at the connecting AC bus by providing the necessary reactive power compensation.

5. CASE STUDY AND RESULTS

A generic, five-bus network is used as the base test case network (Figure 6.1) for testing the performance of the N-R power flow algorithm. Note that this test network may represent either a high-voltage power transmission system or a future low-voltage power distribution system, with a meshed structure for improved reliability of supply and with embedded generation. The network parameters are given in per-unit.

In the original network, there are five buses, four loads, two synchronous generators and seven transmission lines. Buses are denoted as 1, 2, 3, 4 and 5. Loads are connected at node-2, node-3, node-4 and node-5. The network parameters and load data of the original five-bus network are given in Table 5.1 and Table 5.2, respectively.

Table 5.1 : Transmission lines data

Transmission lines	Resistance,R (p.u)	Reactance,X (p.u)	Susceptance,B (p.u)
TL-1	0.02	0.06	0.06
TL-2	0.08	0.24	0.05
TL-3	0.06	0.18	0.04
TL-4	0.06	0.18	0.04
TL-5	0.04	0.12	0.03
TL-6	0.01	0.03	0.02
TL-7	0.08	0.24	0.05

Table 5.2: Loads data

Nodes	Active power (p.u.)	Reactive power (p.u.)
2	0.20	0.10
3	0.45	0.15
4	0.40	0.05
5	0.60	0.10

5.1 Power flows in the original network

The power flow results for the original network are shown on Figure 5.1. The nodal voltage solution is given in Table 5.3 for all five buses and active and reactive power flows and losses are given in Table 5.4 for all seven transmission lines.

In this solution case, bus-1 and bus-2 are considered as slack bus and generator bus, respectively. The rest of the buses are counted as load buses. Initially, voltage magnitude and phase angle for all the buses are taken to be 1p.u. and 0 degree except for bus-1, which is 1.06p.u. and 0 degree for its phase angle. The set active power for generator is 0.2p.u. and its upper and lower reactive power limits are set at +5p.u. to -5p.u., respectively. The power flow solution does not require that the active and reactive powers of the Slack node be specified at any particular value. The N-R algorithm takes 4 iterations to converge, fulfilling the power mismatch tolerance of $1e^{-12}$.

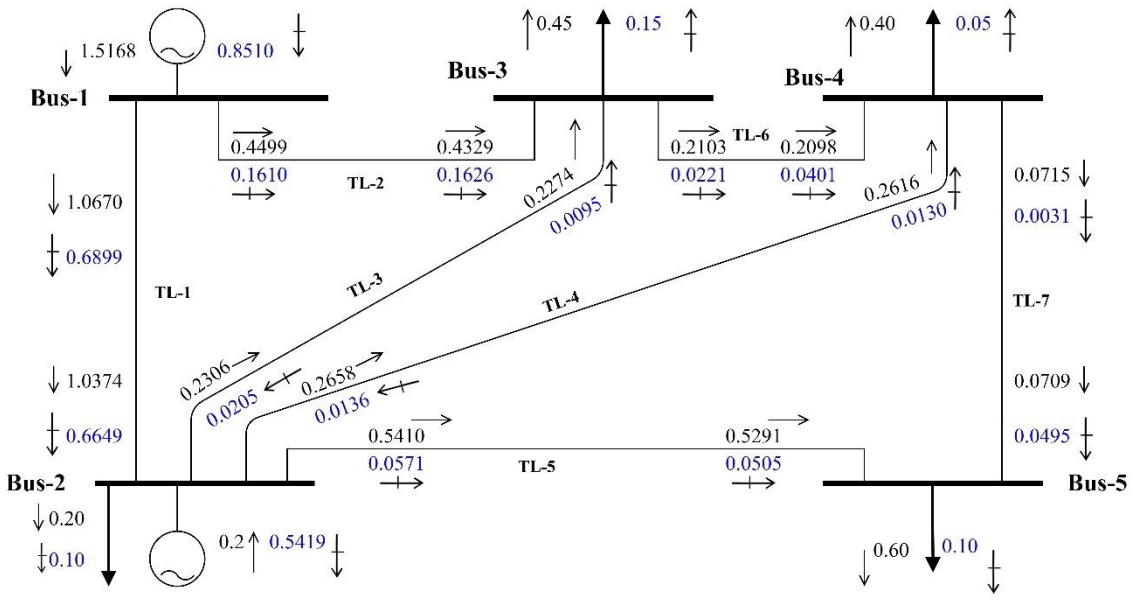

Figure 5.1: Power flows in the original network

Table 5.3: Voltage profile of the original network.

Nodal Voltages	Bus-1	Bus-2	Bus-3	Bus-4	Bus-5
Magnitude (p.u.)	1.0600	1.0000	0.9871	0.9840	0.9717
Phase-angle (degree)	0	-2.6790	-5.0903	-5.4437	-6.3395

Table 5.4 : PQ losses in transmission lines

Transmission line	Sending end power	Receiving end power	PQ losses
TL-1	1.0670 + 0.6899i	-1.0374 - 0.6649i	0.0296 + 0.0250i
TL-2	0.4499 + 0.1610i	-0.4329 - 0.1626i	0.0170 - 0.0016i
TL-3	0.2306 - 0.0205i	-0.2274 - 0.0095i	0.0032 - 0.0299i
TL-4	0.2658 - 0.0136i	-0.2616 - 0.0130i	0.0042 - 0.0266i
TL-5	0.5410 + 0.0571i	-0.5291 - 0.0505i	0.0119 + 0.0066i
TL-6	0.2103 + 0.0221i	-0.2098 - 0.0401i	0.0005 - 0.0180i
TL-7	0.0714 + 0.0031i	-0.0709 - 0.0495i	0.0005 - 0.0464i

Below, there are two test cases, where the original network is expanded to incorporate wind farms using HVDC links. These preliminary studies enable to examine the active power and voltage control capabilities of the VSC-HVDC link in the realm of wind farm power evacuation.

5.2 Power flows in the modified network: Test Case 1

In Test Case-1, the original five-bus network is modified to become a six-bus network in order to incorporate a two-level, VSC-HVDC link connected at bus-2 and bus-6. PMSG-based and SCIG-based wind farms are connected at bus-6 and bus-5, respectively. The number of WT are twenty in each wind farm. The nominal power of a WT is 0.014 p.u. on a power base of 100 MVA. The base voltage is 15kV. As initial conditions, the PMSG's internal voltages are set at 1 p.u. magnitude and 0 phase angle and slip values of the SCIGs are set at -0.01.

The converter station VSC-2 which is connected at node-6, acts as a rectifier and is set to regulate active power at its DC bus at 0.27 p.u. The converter station VSC-1 which is connected at node-2, acts as inverter and is set to regulate voltage magnitude at bus-2 at 1 p.u. Since the converter power losses are unknown prior to the solution, a battery is added at bus-6 to supply such power loss. Power flows throughout the modified power grid are shown on Figure 5.2. The solution converged after 5 iterations.

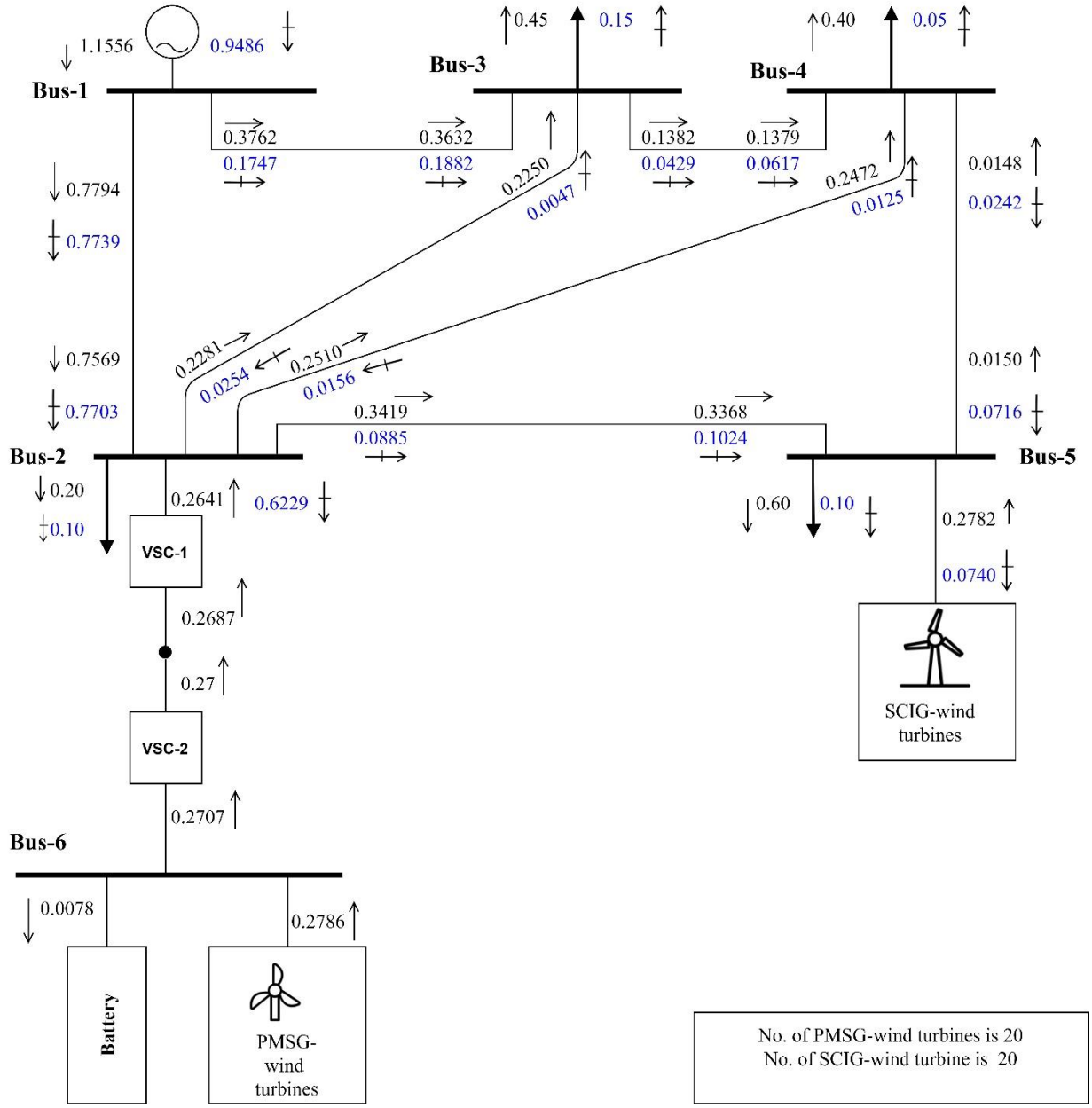

Figure 5.2: Power flows - when a PMSG-based wind farm and battery are connected at bus-6 and a HVDC link connects bus 6 and bus 2 and a SCIG-based wind farm is directly connected at bus 5.

From figure-6.2, it can be seen that VSC-2 experiences 0.07% of active power losses due to switching and conduction losses and delivers 0.27p.u. active power to the rectifier's DC side. The battery consumes 0.0078 p.u. of active power and provides reactive power compensation (0.0014 p.u.) to VSC-2. The PMSG-WF injects 0.2786 p.u. of active power at bus-6 and its internal voltage magnitude and phase angle are: 1.0038 p.u. and 1.4852 degrees, respectively. The SCIG-WF generates 0.2782 p.u. active power and consumes 0.0740 p.u. reactive power, having a slip of -0.6378% and 0.9694 lagging power factor.

The converter station VSC-1 injects 0.2641 p.u. active power to the grid and its associated active power losses due to switching and conduction losses are 0.46%.

The series resistance and reactance of the two converters are 0.002 p.u. and 0.010 p.u., respectively. The shunt conductance is 0.002 p.u. The nodal voltage profile of the modified power network is presented in Table 5.5.

Table 5.5: Voltage profile of Test Case 1

Nodal Voltages	Bus-1	Bus-2	Bus-3	Bus-4	Bus-5	Bus-6
Magnitude (p.u.)	1.0600	1.0000	0.9882	0.9852	0.9746	0.9986
Phase-angle (degree)	0	-1.6548	-4.0549	-4.2679	-3.8241	1.1499

The converter station VSC-1 consumes 0.6229 p.u of reactive power from the grid to maintain the voltage magnitude at 1p.u at bus-2. The internal voltage of the battery is 1.02 p.u. All voltage magnitudes are within the acceptable range (0.95-1.05 p.u.).

The power flows and losses in all seven transmission lines are given in Table 5.6 whereas the converter stations operational parameters are given in Table 5.7.

Table 5.6: Power flows and losses in transmission lines of Test Case 1

Transmission line	Sending end power	Receiving end power	PQ losses
TL-1	0.7794 + 0.7739i	-0.7569 - 0.7703i	0.0224 + 0.0036i
TL-2	0.3762 + 0.1747i	-0.3632 - 0.1882i	0.0130 - 0.0135i
TL-3	0.2281 - 0.0254i	-0.2250 - 0.0047i	0.0031 - 0.0302i
TL-4	0.2510 - 0.0156i	-0.2472 - 0.0125i	0.0038 - 0.0281i
TL-5	0.3419 + 0.0885i	-0.3368 - 0.1024i	0.0051 - 0.0139i
TL-6	0.1382 + 0.0429i	-0.1379 - 0.0617i	0.0002 - 0.0188i
TL-7	-0.0148 + 0.0242i	0.0150 - 0.0716i	0.0002 - 0.0474i

Table 5.7 : VSC parameters in Test Case 1

Converters parameters	VSC-1	VSC-2
Modulation index, m_a	0.8118	0.8144
Internal phase angle, φ	-1.4308	1.0426
Equivalent susceptance, B_{eq}	-0.6254	-0.007

5.3 Power flows in the modified network: Test Case 2

The original five-bus network is further modified to include seven nodes. Like Test Case 1, twenty PMSG-based wind turbines and one battery are connected at bus-6. A VSC-HVDC links buses 2 and 6. Addition to this, another PMSG-WF is placed at bus-7 along with a battery facility and a VSC-HVDC is connecting bus-5 and bus-7. The NR-power flow takes 6 iterations to converge to the power mismatch tolerance of $1e^{-12}$.

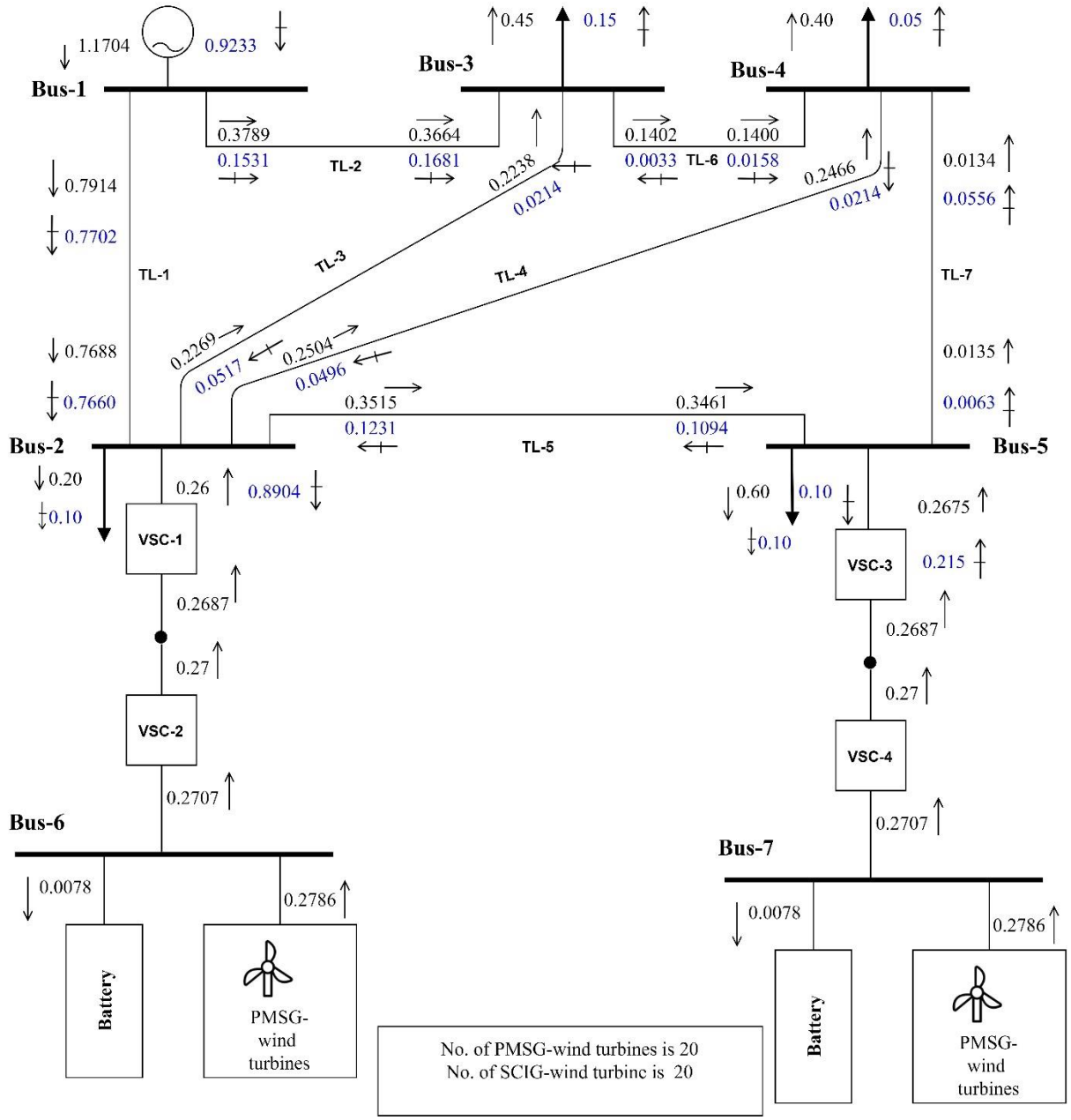

Figure 5.3: Power flows when a PMSG-based wind farm and batteries are connected at bus-6 and bus-7 using VSC-HVDC links.

It can be seen from Figure 5.3 that the converter stations VSC-2 and VSC-4 experience the same amount of active power losses, 0.07% due to switching and conduction losses, and that both deliver 0.27p.u. active power to their respective DC buses. The PMSG-WFs inject 0.2786 p.u. of active power at bus-6 and bus-7. The internal voltage magnitudes and phase angles of the PMSGs are 1.0038 p.u. and 1.4852 degree, respectively. Each battery consumes 0.0078 p.u. of active power and compensated 0.0014 p.u. of reactive power to VSC-2 and VSC-4. The converter station VSC-1 injects 0.26 p.u. of active power to the grid and their associated active power losses due to switching and conduction losses is 0.87%. At bus-5, the active power injected to the network by VSC-

3 is 0.2675 p.u. where the active power losses are 0.12% at VSC-3. The voltage profile at all seven nodes are given in Table 5.8.

Table 5.8: Nodal voltage profile (Test Case 2)

Nodal Voltages	Bus-1	Bus-2	Bus-3	Bus-4	Bus-5	Bus-6	Bus-7
Magnitude (p.u.)	1.0600	1.0000	0.9930	0.9914	1.00	0.9986	0.9986
Phase-angle (degree)	0	-1.6978	-4.1653	-4.4062	-4.3632	1.1980	1.1980

In this test case as well, all the voltage magnitudes are within an acceptable range (0.95-1.05 p.u.). It can be seen that all converters are capable of regulating voltage magnitude by either consuming or injecting reactive power from or into to the grid. VSC-1 consumes 0.8904 p.u. of reactive power from the grid to maintain the voltage magnitude at 1p.u. whereas VSC-3 generates 0.215 p.u. of reactive power in order to keep the voltage magnitude at 1p.u. at bus-5. The internal voltage of the battery is 1.02 p.u.

The power flows and losses in all seven transmission lines are given in Table 5.9 whereas the converter stations operational parameters are given in Table 5.10.

Table 5.9 : Power flows and losses in transmission lines for Test Case 2

Transmission line	Sending end power	Receiving end power	PQ losses
TL-1	0.7914 + 0.7702i	-0.7688 - 0.7660i	0.0227 + 0.0043i
TL-2	0.3789 + 0.1531i	-0.3664 - 0.1681i	0.0126 - 0.0151i
TL-3	0.2269 - 0.0517i	-0.2238 + 0.0214i	0.0032 - 0.0303i
TL-4	0.2504 - 0.0496i	-0.2466 + 0.0214i	0.0038 - 0.0281i
TL-5	0.3515 - 0.1231i	-0.3461 + 0.1094i	0.0054 - 0.0138i
TL-6	0.1402 - 0.0033i	-0.1400 - 0.0158i	0.0002 - 0.0191i
TL-7	-0.0134 - 0.0556i	0.0135 + 0.0063i	0.0001 - 0.0493i

Table 5.10 : VSC parameters in Test Case 2

Converters parameter	VSC-1	VSC-2	VSC-3	VSC-4
Modulation index, m_a	0.8097	0.8144	0.8187	0.8144
Internal phase angle, φ	-1.4447	1.0426	-4.2350	1.0426
Equivalent susceptance, B_{eq} (p.u.)	-0.8968	-0.007	0.2157	-0.007

5.4 Conclusion

Power flows studies of two different cases using VSC-HVDC model with wind farm has been comprehensively observed. It is clearly visible that the action of VSC-HVDC links provide an improved voltage profile in all buses. Inferencing the total power losses in the transmission lines are presented in Table 5.11.

Table 5.11 : Total active and reactive losses in transmission lines for different cases

Cases	Active and reactive power losses
Original network	0.0686-0.0909i
Test Case 1	0.0478-0.1483i
Test Case 2	0.048-0.1513i

It is noticed that Test Case1 and Test Case 2 incur 2.08% and 2.06% less active power losses compared to the base network. It should also be noticed the total active and re-active power losses in the VSC power stations for Test Case 1 and Test Case 2 are 0.0532 + 0.4760i and 0.0591 + 0.5261i, respectively. However, and as key conclusion, it can be said that two-level, VSC-HVDC links are amenable to reduced power losses in the totality of the power grid.

6. CONCLUSIONS AND FURTHER WORK

6.1 Conclusions

The main objective of this research work was to examine the controllability of the steady-state voltage and active and reactive power flows of VSC-HVDC links when connecting wind farms into the power grid. The general conclusion is that VSC-HVDC can be effectively used to regulate the voltage to healthy levels and to control power flows to minimize the transmission power losses. The detailed theoretical background and the simulation results carried out support this main conclusion.

In the designed part of VSC-HVDC link model, different types of switches and HVDC link schemes and their possible arrangements have been studied thoroughly. It is concluded that IGBT-based, two-level, VSC-HVDC links with PWM control is a suitable and well-developed equipment option to fulfil the objectives contemplated in this research work. Mathematical formulations of back-to-back VSC-HVDC link, PMSG and SCIG wind turbines were developed to perform Newton-Raphson power flow iterative solutions. In the simulation part, using the mathematical models presented earlier in the thesis, incorporated in a MATLAB computing engine, were used to assess the performance of these models.

The simulation results give further assurances that VSC-HVDC links do provide high controllability of active and reactive powers and effective voltage regulation. A corollary to the above is that maximization of DG penetration while minimizing transmission power losses is achievable by using the VSC-HVDC technology.

6.2 Further work

Future research work would be centred in the development of additional mathematical models of wind farm equipment and computer programs to be used in the assessment of large-scale power networks, adding a variety of grid-connected renewable energy resources. It is also envisaged that the use of the basic back-to-back VSC-HVDC model could be further developed to perform fault analysis in multiterminal-VSC-HVDC systems.

REFERENCES

[1] Evolution of HVDC Light, ABB 2018, Available: https://new.abb.com/news/detail/4224/evolution-of-hvdc-lightr.

[2] G. Zhang, Z. Li, B. Zhang, W.A. Halang, Power electronics converters: Past, present and future, Renewable and Sustainable Energy Reviews, Vol. 81, 2018, pp. 2028-2044. http://www.sciencedirect.com/science/article/pii/S1364032117309498.

[3] P. RODRIGUEZ, K. ROUZBEHI, Multi-terminal DC grids: challenges and prospects, Journal of Modern Power Systems and Clean Energy, Vol. 5, Iss. 4, 2017, pp. 515-523. https://search.proquest.com/docview/1921403779.

[4] Vision on Market Design and System Operation towards 2030, ENTSO, https://vision2030.entsoe.eu/wp-content/uploads/2019/11/entsoe_fp_vision_2030_web.pdf.

[5] Global Wind Report 2019, GWEC, https://gwec.net/global-wind-report-2019/.

[6] Nursebo Shemsedin, Maximizing the integration of wind power in distribution system, MSc thesis, Chalmers University of Technology, 2013.

[7] S.M. Muyeen, R. Takahashi, J. Tamura, Operation and Control of HVDC-Connected Offshore Wind Farm, IEEE Transactions on Sustainable Energy, Vol. 1, Iss. 1, 2010, pp. 30-37.

[8] J. Arrillaga, High voltage direct current transmission, 2. ed. ed. Inst. of Electrical Engineers, London, 1998.

[9] K.R. Padiyar, HVDC Power Transmission Systems: Technology and System Interactions, Wiley, 1990.

[10] E.W. Kimbark, Direct Current Transmission, Wiley, 1971.

[11] K. Meah, S. Ula, Comparative Evaluation of HVDC and HVAC Transmission Systems, 2007 IEEE Power Engineering Society General Meeting, IEEE, pp. 1-5.

[12] P.D. Masoud Farzaneh, P.D. Shahab Farokhi, W.A. Chisholm, HVDC Transmission Systems and FACTS Devices, in: Anonymous (ed.), McGraw-Hill Education, New York, 2013.

[13] A. Alassi, S. Bañales, O. Ellabban, G. Adam, C. MacIver, HVDC Transmission: Technology Review, Market Trends and Future Outlook, Renewable and Sustainable Energy Reviews, Vol. 112, 2019, pp. 530-554. https://www.sciencedirect.com/science/article/pii/S1364032119302837.

[14] A. Kalair, N. Abas, N. Khan, Comparative study of HVAC and HVDC transmission systems, Renewable and Sustainable Energy Reviews, Vol. 59, 2016, pp. 1653-1675. https://www.sciencedirect.com/science/article/pii/S1364032115016718.

[15] E. Acha, P. Roncero-Sánchez, A. de la Villa-Jaen, L.M. Castro, B. Kazemtabrizi, Vsc-Facts-hvdc : Analysis, Modelling and Simulation in Power Grids, John Wiley & Sons, Incorporated, Somerset, 2019.

[16] R. Teodorescu, M. Liserre, P. Rodr?guez, Grid Converters for Photovoltaic and Wind Power Systems, 1. Aufl. ed. Wiley-IEEE Press, Hoboken, 2010.

[17] N. Jenkins, N. Jenkins, R. Allan, P. Crossley, D. Kirschen, G. Strbac, Embedded generation, Institution of Engineering and Technology, 2008.

[18] J. MAZA-ORTEGA, E. ACHA, S. GARCÍA, A. GÓMEZ-EXPÓSITO, Overview of power electronics technology and applications in power generation transmission and distribution, Journal of Modern Power Systems and Clean Energy, Vol. 5, Iss. 4, 2017, pp. 499-514.

[19] P. Caramia, P. Caramia, G. Carpinelli, P. Verde, Power quality indices in liberalized markets, WILEY, New York, 2009.

[20] A. Ioinovici, H. Chung, Power Electronics and Energy Conversion Systems, Fundamentals and Hard-Switching Converters : Fundamentals and Hard-Switching Converters, John Wiley & Sons, Incorporated, Somerset, 2013.

[21] T.K. Gachovska, J.L. Hudgins, A. Bryant, P. Palmer, S. Yuvarajan, 3 - Thyristors, in: M.H. Rashid (ed.), Power Electronics Handbook (Fourth Edition), Butterworth-Heinemann, 2018, pp. 49-81.

[22] J. Arrillaga, Self-commutating converters for high power applications, Wiley, Chichester, 2009.

[23] A. Kopta, M. Rahimo, C. Corvasce, M. Andenna, F. Dugal, F. Fischer, S. Hartmann, A. Baschnagel, Next Generation IGBT and Package Technologies for High Voltage Applications, IEEE Transactions on Electron Devices, Vol. 64, Iss. 3, 2017, pp. 753-759. https://ieeexplore.ieee.org/document/7845561.

[24] E. Deng, Z. Zhao, Q. Xin, J. Zhang, Y. Huang, Analysis on the difference of the characteristic between high power IGBT modules and press pack IGBTs, Microelectronics Reliability, Vol. 78, 2017, pp. 25-37. https://www.sciencedirect.com/science/article/pii/S0026271417303876.

[25] Press-pack IGBT and diode modules, http://search.abb.com/library/Download.aspx?DocumentID=5SYA1467&LanguageCode=en&DocumentPartId=&Action=Launch.

[26] Press-Pack IGBT Capsules, http://www.westcode.com/igbt1.html.

[27] Press-Pack package, https://toshiba.semicon-storage.com/us/semiconductor/product/high-power-devices/iegt-ppi/press-pack-package.html.

[28] Press-pack IGBT , https://www.dynexsemi.com/assets/downloads/4.5kV_Press_Pack_IGBT_Overview_.pdf.

[29] W. Zhang, G. Asplund, A. Aberg, U. Jonsson, O. Loof, Active DC filter for HVDC system-a test installation in the Konti-Skan DC link at Lindome converter station, IEEE Transactions on Power Delivery, Vol. 8, Iss. 3, 1993, pp. 1599-1606.

[30] E. Acha, Flexible Transmission System, Lecture Notes # 3: VSC-HVDC Power Converters and Systems, Tampere University, 2019.

[31] N. Mohan, Power electronics : converters, applications, and design, United States, 2003.

[32] N. Flourentzou, V.G. Agelidis, G.D. Demetriades, VSC-Based HVDC Power Transmission Systems: An Overview, IEEE Transactions on Power Electronics, Vol. 24, Iss. 3, 2009, pp. 592-602. https://ieeexplore.ieee.org/document/4773229.

[33] J. Rodriguez, Jih-Sheng Lai, Z.P. Fang, Multilevel inverters: a survey of topologies, controls, and applications, IEEE Transactions on Industrial Electronics, Vol. 49, Iss. 4, 2002, pp. 724-738.

[34] N. Ahmed, A. Haider, D. Van Hertem, L. Zhang, H. Nee, Prospects and challenges of future HVDC SuperGrids with modular multilevel converters, Proceedings of the 2011 14th European Conference on Power Electronics and Applications, pp. 1-10.

[35] A. Lesnicar, R. Marquardt, An innovative modular multilevel converter topology suitable for a wide power range, 2003 IEEE Bologna Power Tech Conference Proceedings, pp. 6 pp. Vol.3.

[36] S. Allebrod, R. Hamerski, R. Marquardt, New transformerless, scalable Modular Multilevel Converters for HVDC-transmission, 2008 IEEE Power Electronics Specialists Conference, IEEE, pp. 174-179.

[37] E. Acha, T. Rubbrecht, L.M. Castro, Power flow solutions of AC/DC micro-grid structures, 2016 Power Systems Computation Conference (PSCC), pp. 1-6.

[38] Grid code specifications for power generating facilities, https://www.fingrid.fi/globalassets/dokumentit/en/customers/grid-connection/grid-code-specifications-for-power-generating-facilities-vjv2018-.pdf.

[39] M.R. Hazari, M.A. Mannan, A. Umemura, R. Takahashi, J. Tamura, Stabilization of Wind Farm by Using PMSG Based Wind Generator Taking Grid Codes into Consideration, Journal of power and energy engineering, Vol. 6, Iss. 11, 2018, pp. 40-52.

[40] M.R. Hazari, E. Jahan, M.A. Mannan, J. Tamura, Coordinated Control Scheme of Battery Storage System to Augment LVRT Capability of SCIG-Based Wind Turbines and Frequency Regulation of Hybrid Power System, Electronics (Basel), Vol. 9, Iss. 2, 2020, pp. 239.

[41] Q. Wu, Y. Sun, Modeling and modern control of wind power, John Wiley & Sons, Hoboken, NJ, https://onlinelibrary.wiley.com/doi/book/10.1002/9781119236382.

APPENDIX: SYSTEM PERAMETERS

VSC-HVDC link data				
Parameters	VSC-1	VSC-2	VSC-3	VSC-4
Series resistance (p.u.)	0.002	0.002	0.002	0.002
Series reactance (p.u.)	0.010	0.010	0.010	0.010
Initial shunt conductance (p.u.)	0.002	0.002	0.002	0.002
Initial equivalence susceptance (p.u.)	1.0	1.0	1.0	1.0
Initial voltage amplitude modulation index	1.0	1.0	1.0	1.0
Internal phase angle (degree)	0.0	0.0	0.0	0.0

SCIG data	
Parameters	Values
Initial slip, s (%)	0.01
Stator winding resistance, R_S (Ω)	2.1
Rotor winding resistance, R_r (Ω)	0.85
Core resistance, R_C (Ω)	1250
Stator leakage reactance, X_S (Ω)	12.97
Rotor leakage reactance, X_r (Ω)	16.49
Magnetizing reactance, X_m (Ω)	413.5

PMSG data	
PMSG parameters	Values, (Ω)
Resistance, R	0.8358
Reactance, X_d	0.6987
Reactance, X_q	0.8056

Data for battery	
Resistance (p.u.)	0.01
Reactance (p.u.)	0.01